SHORT-PITCH PERIODICALLY POLED LITHIUM NIOBATE AND LITHIUM TANTALATE

Period May 1, 1999 to October 31, 1999

Final Report

sponsored by

The European Office of Aerospace R&D

Air Force Office of Scientific Research

Air Force Research Laboratory

Contract N F61775-99-WE037

(SPC-99-4037)

Vladimir Ya. Shur

Report Date: 31/10/99

INSTITUTE OF PHYSICS & APPLIED MATHEMATICS

URAL STATE UNIVERSITY

EKATERINBURG, RUSSIA

REPORT DOCUMENTATION PAGE

Form Approved OMB No. 0704-0188

1. AGENCY USE ONLY (Leave blank)	2. REPORT DATE	3. REPORT TYPE AND DATES COVERED
	1999	Final Report

4. TITLE AND SUBTITLE

Short-Pitch Peiodically Poled Lithium-Niobate And Lithium Tantalate

5. FUNDING NUMBERS

F61775-99-WE037

6. AUTHOR(S)

Prof. Vladimir Ya. Chour

7. PERFORMING ORGANIZATION NAME(S) AND ADDRESS(ES)

Ural State University
Lenin Ave. 51,
Ekaterinburg 620083
Russia

8. PERFORMING ORGANIZATION REPORT NUMBER

N/A

9. SPONSORING/MONITORING AGENCY NAME(S) AND ADDRESS(ES)

EOARD
PSC 802 BOX 14
FPO 09499-0200

10. SPONSORING/MONITORING AGENCY REPORT NUMBER

SPC 99-4037

11. SUPPLEMENTARY NOTES

12a. DISTRIBUTION/AVAILABILITY STATEMENT

Approved for public release; distribution is unlimited.

12b. DISTRIBUTION CODE

A

13. ABSTRACT (Maximum 200 words)

This report results from a contract tasking Ural State University as follows: The contractor will further investigate the back-switched poling method for periodic domain patterning with shorter domain periods in thick lithium niobate and lithium tantalate substrates.

14. SUBJECT TERMS

EOARD, Photonics, Periodic poling, Harmonic generation

15. NUMBER OF PAGES

63

16. PRICE CODE

N/A

17. SECURITY CLASSIFICATION OF REPORT	18. SECURITY CLASSIFICATION OF THIS PAGE	19, SECURITY CLASSIFICATION OF ABSTRACT	20. LIMITATION OF ABSTRACT
UNCLASSIFIED	UNCLASSIFIED	UNCLASSIFIED	UL

CONTENTS

1 ABSTRACT 4

2 INTRODUCTION 4

3 EXPERIMENT 5

3.1 SAMPLES 5

3.1.1 Congruent lithium niobate and lithium tantalate 6

3.1.2 Stoichiometric lithium tantalate prepared by Vapor Transport Equilibration method 6

3.1.3 Stoichiometric lithium tantalate grown by double crucible Czochralski method 7

3.2 EXPERIMENTAL SETUP FOR DOMAIN PATTERNING 7

3.3 OPTICAL VISUALIZATION OF THE DOMAIN PATTERNS WITHOUT ETCHING 8

3.4 HIGH-RESOLUTION VISUALIZATION OF NANODOMAINS 9

3.4.1 Comparison of SFM and SEM patterns of etched surface relief 9

3.4.2 Formation of the surface relief during etching 11

3.4.3 Domain observation by SFM in piezoresponse-imaging mode 13

4 MAIN APPROACH TO THE DOMAIN STRUCTURE EVOLUTION 15

5 SWITCHING IN UNIFORM FIELD IN CONGRUENT LITHIUM NIOBATE AND LITHIUM TANTALATE 16

5.1 SWITCHING CURRENT DATA 16

5.2 DOMAIN SHAPE DURING SWITCHING IN LITHIUM TANTALATE 18

5.3 IN SITU OBSERVATION OF THE DOMAIN KINETICS IN LITHIUM NIOBATE 20

5.4 IN SITU OBSERVATION OF THE DOMAIN KINETICS IN LITHIUM TANTALATE 22

5.4.1 Domain evolution 22

5.4.2 "Optical" switching current 26

5.4.3 Simulation of the original domain kinetics observed in congruent lithium tantalate 28

6 POLARIZATION REVERSAL IN STOICHIOMETRIC LITHIUM TANTALATE 29

6.1 DOMAIN STRUCTURE AND SWITCHING IN VAPOR TRANSPORT EQUILIBRATION LITHIUM TANTALATE 29

6.1.1 As-grown domain structure with charged domain walls and twins 30

6.1.2 Switching currents and hysteresis loops 33

6.2 DOMAINS AND SWITCHING CURRENTS IN LITHIUM TANTALATE GROWN BY DOUBLE CRUCIBLE CZOCHRALSKI METHOD 34

7 FORMATION AND EVOLUTION OF CHARGED DOMAIN WALLS IN CONGRUENT LITHIUM NIOBATE 36

7.1 FORMATION OF THE CHARGED DOMAIN WALL 36

7.2 SIDEWAYS MOTION OF NEUTRAL DOMAIN WALL 37

7.3 FIELD INDUCED EVOLUTION OF THE CHARGED DOMAIN WALL 38

8 PERIODICAL DOMAIN PATTERNING IN CONGRUENT LITHIUM NIOBATE AND LITHIUM TANTALATE 39

8.1 DOMAIN SHAPE DURING PATTERNING IN LITHIUM NIOBATE 39

8.2 DOMAIN SHAPE DURING PATTERNING IN LITHIUM TANTALATE 41

8.3 SPREADING OF THE DOMAIN WALLS OUT OF THE ELECTRODES IN LITHIUM NIOBATE 41

8.3.1 Finger assisted domain wall motion 41

8.3.2 Switching current during patterning in lithium niobate with current limitation 42

8.3.3 Calculation of the domain wall spreading out of the electroded area 44

8.4 DOMAIN WALLS INTERACTION DURING COALESCENCE 46

8.5 FREQUENCY MULTIPLICATION OF PERIODICAL DOMAIN PATTERNS 47

9 NANODOMAIN ENGINEERING IN LITHIUM NIOBATE 49

9.1 FORMATION OF PERIODIC STRIP NANODOMAIN STRUCTURES 51

9.2 FORMATION OF THE QUASI-PERIODICAL STRUCTURE OF ORIENTED NANODOMAIN ARRAYS 51

9.3 PHYSICAL BASIS OF NANODOMAIN ENGINEERING 53

9.4 CORRELATED NUCLEATION UNDER THE ELECTRODE EDGES 54

9.5 MECHANISM OF CORRELATED NUCLEATION 55

10 SHORT-PITCH DOMAIN PATTERNS IN LITHIUM NIOBATE AND LITHIUM TANTALATE 57

10.1 APPLICATION OF THE BACKSWITCHED POLING FOR 2.6 μM PATTERNING IN LITHIUM NIOBATE 57

10.2 QUASI-PHASEMATCHED GENERATION IN BACKSWITCHED-POLED LITHIUM NIOBATE 58

10.3 2.6 μM PATTERNING IN LITHIUM TANTALATE 59

11 RECOMMENDATION 59

12 REFERENCES 60

PRESENTATIONS 62

1 Abstract

We enhance the recently proposed by us original backswitched poling method for periodic domain patterning with shorter domain periods in thicker $LiNbO_3$ (LN) and $LiTaO_3$ (LT) substrates, which are important for quasi-phasematched nonlinear optics. We investigate in details the domain evolution at the different stages of backswitching process especially the formation of the nanoscale domain structures. The main attention has been paid to the nucleation of new domains and sideways motion of the domain walls. The self-organized formation of the strictly oriented nanoscale domain arrays has been observed for the first time. We compare the domain kinetics and switching parameters for conventional congruent LT single crystals and stoichiometric ones produced by Vapor Transport Equilibration and grown by double crucible Czochralski method.

2 Introduction

Recently a new branch of ferroelectric technology and science named **domain engineering** has been developing rapidly. The target of this activity is to find ways of producing desired domain structures with precise reproducibility of the main parameters in commercially available ferroelectric materials. The particular attention is paid to periodically poled lithium niobate, lithium tantalate and KTP family crystals which had a major impact on nonlinear optical frequency conversion. Ferroelectric domain engineering is important for quasi-phasematched (QPM) nonlinear optics [1]. For QPM interactions involving visible and ultraviolet (UV) wavelengths, the dispersion characteristics of common nonlinear crystals require short-period domain gratings. To date, the creation of the domain periods of 3-4 microns in 0.2-0.3-mm-thick substrates have been reported for electric-field-poled LT [2,3], LN [4,5] and KTP [6]. Such progress shows promise for the second harmonic generation (SHG) of blue [2,6] and even UV light [3]. Nevertheless, in thicker substrates, difficulties remain in the reproducible fabrication of uniform quality QPM materials for visible and UV wavelengths. With the proper voltage waveform and surface preparation, 6.5-micron-period uniform domain structures, having controlled duty cycle, can be formed throughout 76-mm-diameter 0.5-mm-thick LN wafers [7]. While such a QPM period is useful for first-order SHG of green light, first-order SHG of blue and UV light requires shorter periods. Detailed study of the physical nature of nucleation, evolution and stabilization of the domain patterns is required to solve this problem. It must be stressed that complex studying of domain evolution during polarization reversal is of principal importance for improving the domain patterning in LN and LT.

It is well known that in ferroelectrics after fast removing of the external electric field the created domain structure becomes unstable and partial spontaneous reconstruction of the initial domain state ("backswitching" or "flip-back") is usually observed. However the domain evolution during this spontaneous decay is practically unstudied. It was shown only that the characteristic time of this process strongly depends on material and experimental conditions [8-10]. Recently the new method of short-period domain structure fabrication based on the effect of spontaneous backswitching was proposed and realized in LN. The further development of this method demands the thoroughly investigation of the evolution of domain kinetics during spontaneous backswitching.

The backswitching is governed by the superposition of the partly compensated depolarization field and residual bulk field, which was compensating the external field [11-13]. These backswitching fields decrease with time, but just after fast field removing they can sufficiently exceed the experimentally produced switching fields. Thus, the high degree of nonequilibrium can be achieved in proper ferroelectrics by choosing optimal experimental conditions. It is clear that effective bulk screening, which determines the backswitching effect, in turn hampers the polarization reversal and increases the threshold fields.

It was shown experimentally that spontaneous decay of highly non-equilibrium domain state in LN is achieved through the formation of self-organized structures consisting of oriented nanodomain arrays with sizes of smallest individual domains less than 50 nm. These structures demonstrate the record value of domain density ever observed (up to 100 μm^2). This also means formation of a great number of charged domain walls in the surface area. Thus it was opened a new field of application of LN in domain engineering through the fabrication of nanodomain structures with high density of domain walls. The investigation of mechanisms of self-maintaining correlated nucleation is very important.

3 Experiment

3.1 Samples

We have investigated in details the domain kinetics during polarization reversal in the conventional single crystals of congruent lithium niobate (CLN) and congruent lithium tantalate (CLT) and also in one of the most promising nonlinear optical material stoichiometric lithium tantalate SLT. The commercially grown crystals are typically produced through an incongruent process. The conventional CLT crystals should contain considerably large amounts of Ta antisite defects and cation vacancies. Recently several methods of preparation of "stoichiometric" LT

crystals are under development. We have studied the samples prepared by two different techniques: 1) high temperature treatment - Vapor Transport Equilibration method (VTE LT) and 2) crystal growth using double crucible Czochralski method (SLT).

3.1.1 Congruent lithium niobate and lithium tantalate

The periodic bulk domain structures were obtained in standard optical-grade single-domain 0.5-mm-thick CLN and 0.3-mm-thick CLT wafers of congruent composition cut normal to polar axis. The wafers were photolithographically patterned with periodic strip metal-electrode structure (NiCr) deposited on $\mathbf{Z}^+$ surface only. The electrodes in CLN were oriented strictly along **Y** axe (one of $[\bullet\bullet\bar{\bullet}\bullet]$ directions). The patterned surface was covered by a 1 μm-thick insulating layer (photoresist or spin-on-glass) to inhibit domain spreading out of electrodes (Fig. 1).

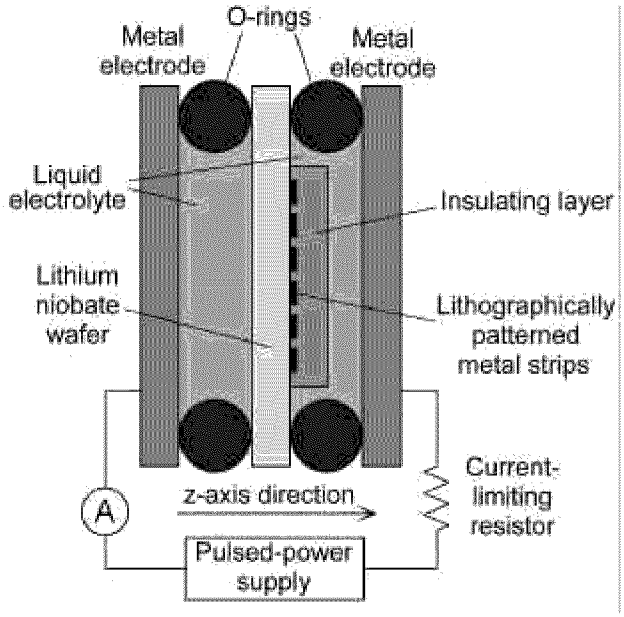

Figure 1 Scheme of the experimental setup for poling.

For *in situ* investigation of the domain kinetics in uniform electric field we have used one-mm-diameter circular transparent electrodes of two types: 1) liquid electrolyte (water solution of LiCl) in special fixture, and 2) In_2O_3:Sn films deposited by magnetron sputtering.

3.1.2 Stoichiometric lithium tantalate prepared by Vapor Transport Equilibration method

Vapor Transport Equilibration method allows to produce the stoichiometric samples by high-temperature treatment of the plates of conventional CLT. The method is rather simple and potentially cheap. The wafers of CLT with sizes about 20x15x1 mm^3 have been treated at the constant temperature in the range 1120 - 1370^{O}C for 100-200 hours in a platinum crucible over a mixture of Li_3TaO_4 and $LiTaO_3$ and controlled O_2 atmosphere [14] The samples have been

polished after treating. It was shown that all of them contain complicated as-grown domain structure with charged domain walls. Moreover all samples annealed at temperatures above 1300^{O}C contain the twin structure.

3.1.3 Stoichiometric lithium tantalate grown by double crucible Czochralski method

SLT crystals with high quality and homogeneity were grown using the double crucible Czochralski method equipped with an automatic powder supply system by K. Kitamura and Y. Furukawa (NIRIM, Tsukuba, Japan) [15,16]. We have investigated single-domain samples cooled in electric field through the transition point. The part of as-grown crystal was annealed in air at 750^{O}C and cooled down at a rate of 2K/min to the room temperature applying a dc electric field along polar direction. The investigated polished plates with thickness about 0.5 - 1 mm have been oriented normal to polar axis.

3.2 Experimental setup for domain patterning

A high voltage pulse producing an electric field greater than the threshold ("coercive") field (21.5 kV/mm) was applied to the electrode structure through the fixture containing a liquid electrolyte (LiCl) [17,18]. The voltage pulse shape controls the parameters of the obtained domain structure (Fig. 2). The voltage waveform consists of three field levels: 1) "high field", 2) "low field", 3) "stabilization field". The switching takes place at the "high field" stage and the backswitching occurs during the "low field" one. The crucial parameters for backswitching kinetics are the duration of "high field" stage Δt_{sp} and the value of the jump from "high" to "low" field (field diminishing amplitude) ΔE. Voltage and current were monitored during polarization reversal.

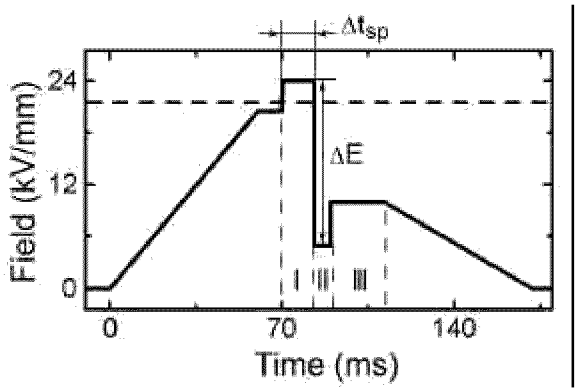

Figure 2 Backswitched poling voltage waveform.

The comparison of domain patterns obtained for different duration of the "low field" stage yields information about domain development during backswitching. For observation of the domain patterns after partial poling the polar surfaces and polished cross-sections were etched for 5 - 10 minutes by hydrofluoric acid (without heating). The obtained surface relief was visualized

by optical microscope or by high-resolution microscopes SEM and SFM. Studying the domain structure in the bulk by optical method the spatial resolution in **X** direction was enhanced by appropriate tilted cross-sections. It was found that cleavage reveals the domain structure even without etching.

3.3 Optical visualization of the domain patterns without etching

We have demonstrated for the first time that the domain patterns in any LN and LT can be visualized by optical microscope in transmitted and reflected modes without any surface treatment by etching or cleavage. Two modifications of the method have been applied: 1) in polarized light and 2) without polarizer and analyzer.

Observation in transmitted polarized light demonstrates the best contrast under application of weak external field (about 500 V/mm), which can not change the domain structure being far below coercive field. The contrast disappears quickly after external field switching off.

More convenient "nonpolarized light" method has been used for LT and LN (Fig. 3-5). The method needs narrow light beam and small controlled deviation of the beam propagation from the polar axis. The good enough contrast has been obtained during observation of the domains with sizes down to 5 microns.

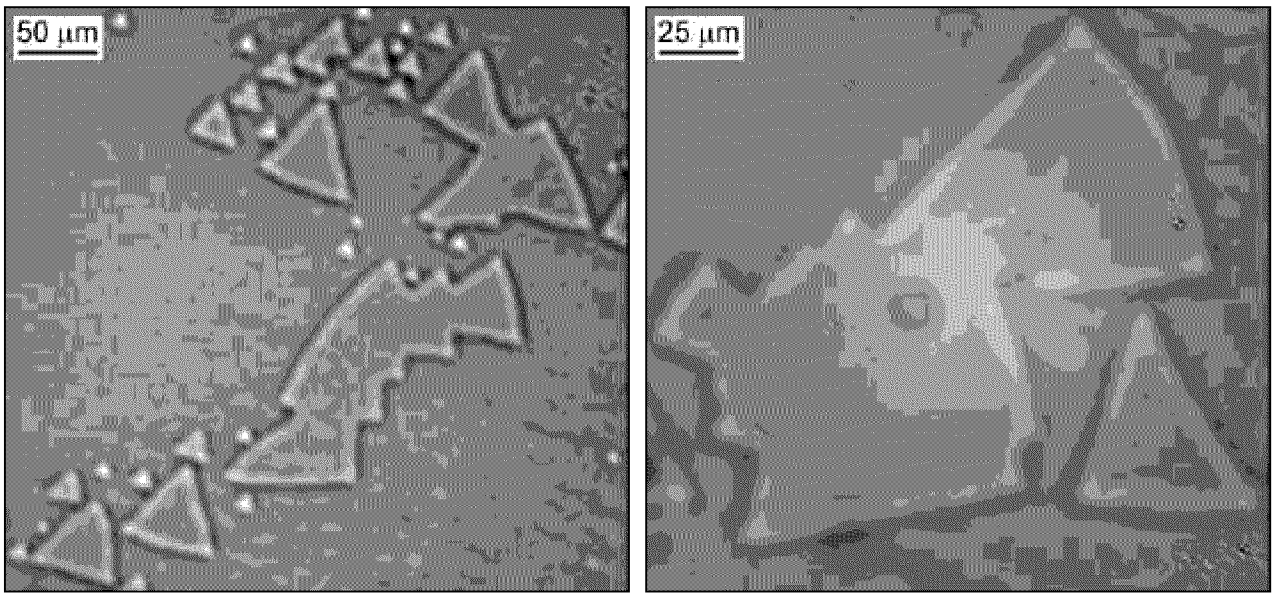

Figure 3 The optical patterns of individual microscale triangular domains in CLT obtained without etching

It must be pointed out that it is easy to control a difference in domain shape between congruent and stoichiometric LT (Fig. 4).

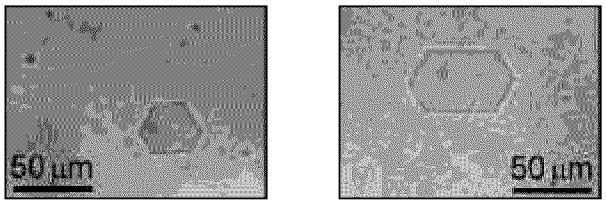

Figure 4 The optical pattern of individual microscale hexagonal domains in SLT obtained without etching

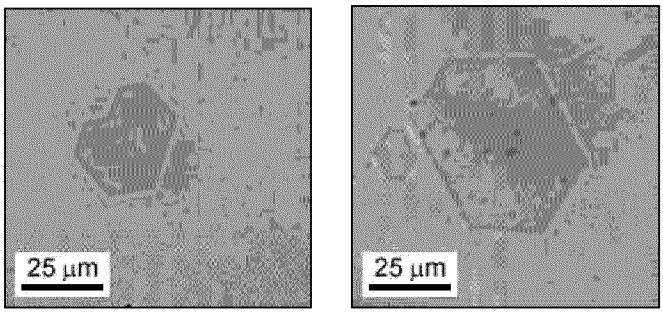

Figure 5 The optical pattern of individual microscale hexagonal domains in SLN obtained without etching

3.4 High-resolution visualization of nanodomains

Additionally to conventional regular micro-scale domain patterns in present research we were studying the nanodomain structures. It is clear that optical observation of such super-small domains is impossible. Thus we apply such high-resolution techniques as Scanning Force Microscopy (SFM) and Scanning Electron Microscopy (SEM).

3.4.1 Comparison of SFM and SEM patterns of etched surface relief

We use the analysis of SEM and SFM patterns associated with etched surface relief as the only sources of knowledge about nanodomains. The reconstruction of the domain patterns from SEM images needs taking into account the distortions caused by etching procedure and peculiarities of SEM observation which are still unsolved problems.

The typical SEM image of etched individual nanodomain and its profile along **Y** direction are presented in Figure 6. It is obvious that size and shape of this nanodomain are unclear from this image. In order to understand the real shape of SEM profile the etching relief in the same sample was checked by SFM (Fig. 7, 8c). It can be seen that the etched hillock has a high gradient near the top and low one at the base (Fig. 7). The hillock height is proportional to the etching time (about 150 nm for 10 minutes).

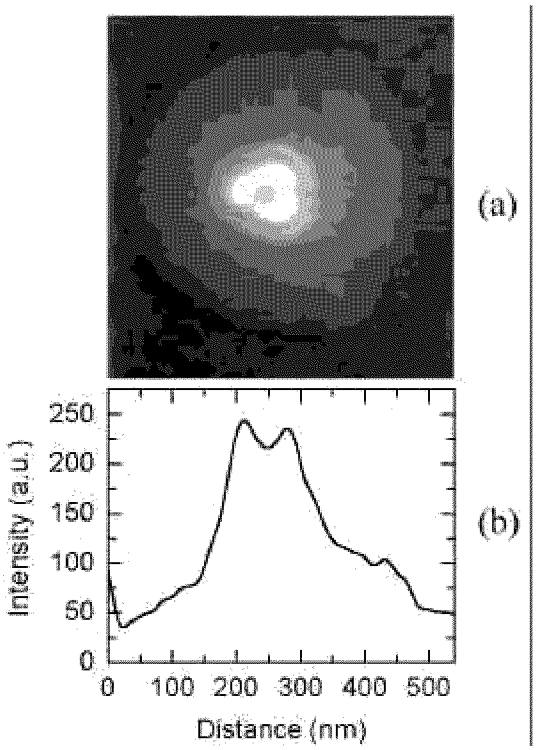

Figure 6 SEM pattern of individual nanodomain in CLN revealed by etching (a) image, (b) profile along **Y** direction

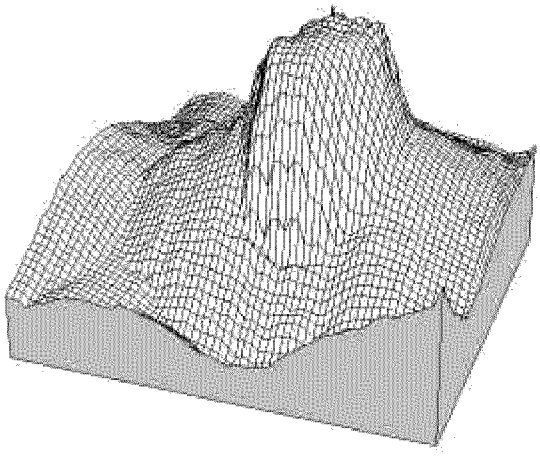

Figure 7 Relief of individual nanodomain in CLN revealed by etching and observed by SFM. Image sizes: 450×400 nm^2, hillock height: 150 nm.

We construct the SEM profile (Fig. 8a) from the relief profile (Fig. 8b) using the following expression for calculation the local SEM signal **I** for normal incidence of electron beam:

$$I \sim \int_S \frac{R}{\cos\theta}\, dS \qquad (1)$$

where **S** - area of electron beam at the sample surface, **R** - maximum escaping depth of secondary electrons, θ - angle between electron beam direction and surface normal vector.

One can find the certain similarities between experimental SEM profile (Fig. 8b) and calculated one (Fig. 8a). In both cases there are two maximums that correspond to steep sides near the top of the hillock. The essential difference between them is due to different slopes of $\mathbf{Y}^+$ and $\mathbf{Y}^-$ sides of hillock due to the anisotropy of etching velocities.

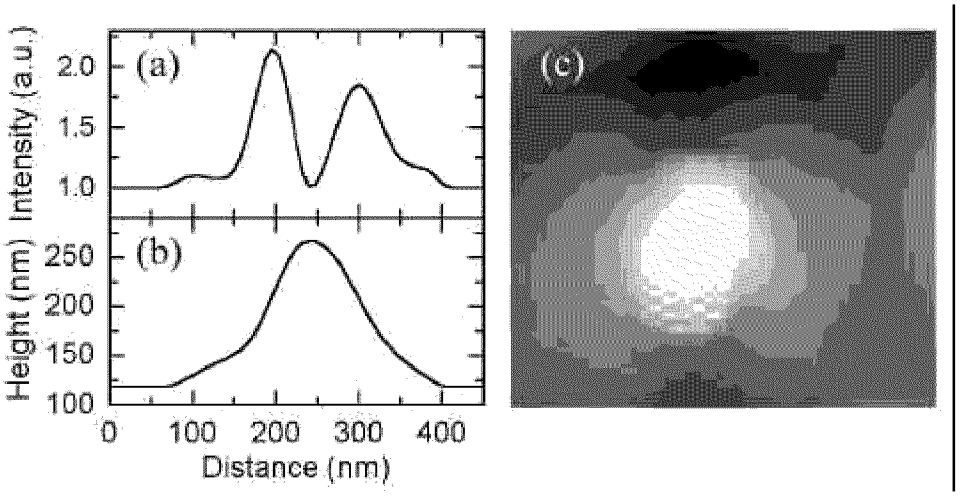

Figure 8 The individual nanodomain pattern in CLN revealed by etching and observed by SFM: (a) – calculated "SEM" profile along **Y** direction obtained from SFM relief profile (b), (c) – SFM pattern.

3.4.2 Formation of the surface relief during etching

It is well known that etching in CLN is a very anisotropic process. The values for etching velocities in main crystallographic directions obtained for etching time from 10 to 40 hours are presented in Table 1.

Table 1. Anisotropy of etching rate in CLN.

Crystallographic directions	Etching rate (nm/hour)
$\mathbf{Z}^+$	96.8
$\mathbf{Z}^-$	0.956
$\mathbf{Y}^+$	74.1
$\mathbf{Y}^-$	1.11
$\mathbf{X}^+$	2.99
$\mathbf{X}^-$	2.98

It is clear that for time about 5 - 10 minutes the etching is important only in $\mathbf{Z}^+$ and $\mathbf{Y}^+$ directions thus it is negligible in any other direction. The essential difference between etching rates in $\mathbf{Z}^-$ and $\mathbf{Z}^+$ directions can be seen on Figure 9 where the etched relief obtained after backswitching under the electrode edges is presented. It appears that the etching rate is nonuniform and depends on distance from the domain wall (Fig. 9).

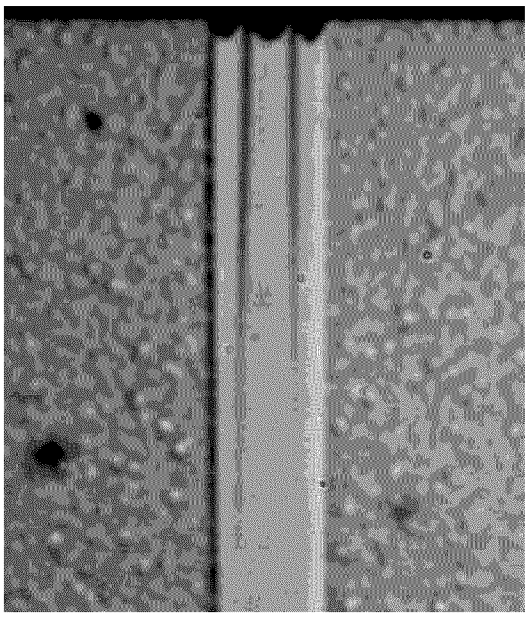

Figure 9 Formation of spike-like domains along electrode edges during backswitching process in CLN. **Y** view of etched relief was visualized by optical microscope. Width of switched lamellar domain is about 2.5 μm.

The anisotropy of etching rate leads to distortion of relief as compare with the shape of nanodomain. The estimated evolution of the relief on $\mathbf{Z}^+$ surface during etching of individual nanodomain with a shape of long hexagon is shown in Figure 10a. One can see that the hillock shape changes in special manner, which is similar to the experimental data.

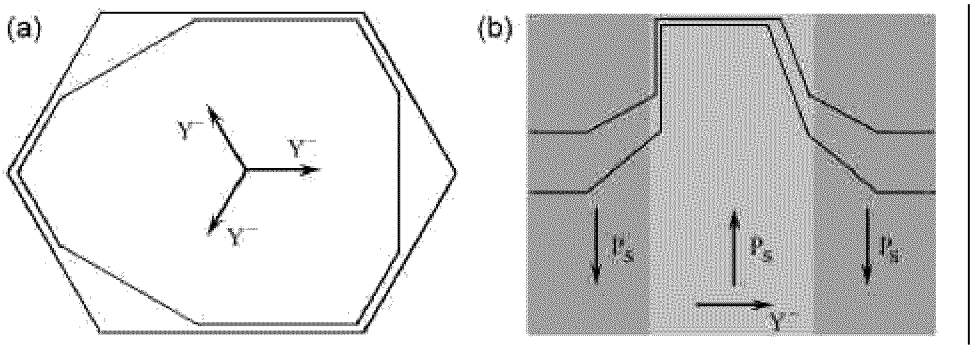

Figure 10 Stages of surface relief evolution during etching of nanodomain in CLN: (a) - **Z** view, (b) - **X** view.

In order to explain the formation of low gradient parts of hillock sides we propose the linear dependence of etching rate $\mathbf{V_Z}$ (in $\mathbf{Z}^-$ direction) on distance $\Delta\mathbf{x}$ from the domain wall:

$$V_Z(\Delta x) = V_{Z\max} - (1 - \frac{\Delta x}{R}) \cdot (V_{Z\max} - V_{Z\min}), \qquad \text{for } \Delta x < R \tag{2}$$

where $\mathbf{V_{Zmax}}$ - etching rate at the distance $\Delta x > R$ from the wall, $\mathbf{V_{Zmin}}$ - etching rate at the wall.

Such dependence can be caused by influence of the local field on the etching rate. Nonuniform field distribution in the vicinity of the domain wall leads to formation of hillock with different gradients near top and base (Fig. 10b). The difference in maximums on SEM profiles can be explained by different etching rate of $\mathbf{Y}^+$ and $\mathbf{Y}^-$ surfaces (Fig. 6b, 8a). Finally we can conclude that the distance between intensity maximums on SEM patterns corresponds to domain sizes as the distance between the points where gradient of hillock sides changes drastically is constant during etching.

3.4.3 Domain observation by SFM in piezoresponse-imaging mode

We successfully apply for the first time the SFM piezoresponse-imaging mode [19,20] for visualization of CLT and CLN domains, working in collaboration with Prof. Levy group from University of Pittsburgh. The SFM piezoresponse-imaging technique [19,20] is based on the detection of the local electromechanical vibration of the ferroelectric sample caused by external ac voltage. The voltage is applied through the probing tip, which is used as a movable top electrode (Fig. 11).

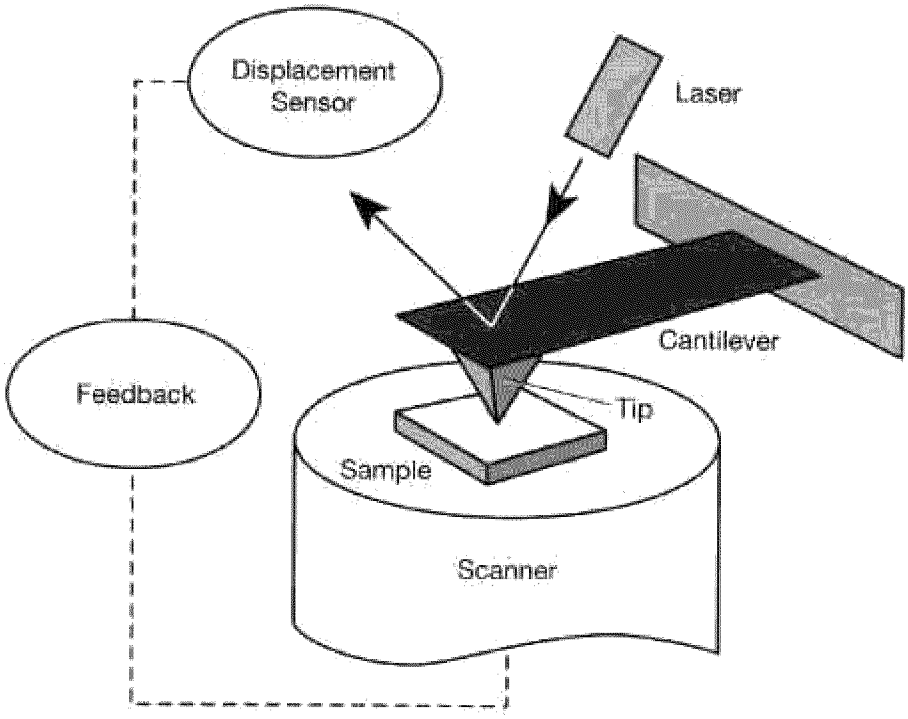

Figure 11 Scheme of a SFM system.

A modulated signal produced by the laser beam reflected from the cantilever, which oscillates together with the sample, is detected using a lock-in technique. In the piezoresponse mode, domain structure can be visualized by monitoring the first harmonic piezoresponse signal. The phase of this signal depends on the sign of the piezoelectric coefficient and therefore on the

direction of spontaneous polarization. This means that regions with opposite orientation of polarization vibrating in counter phase with respect to each other under the applied ac field should appear as regions of different contrast in the piezoresponse image. The method have been demonstrated earlier mostly for ferroelectric thin films [20] We applied that technique to periodically poled CLN sample without electrodes (Fig. 12) and for observation of the domain structure in partly switched CLT (Fig. 13).

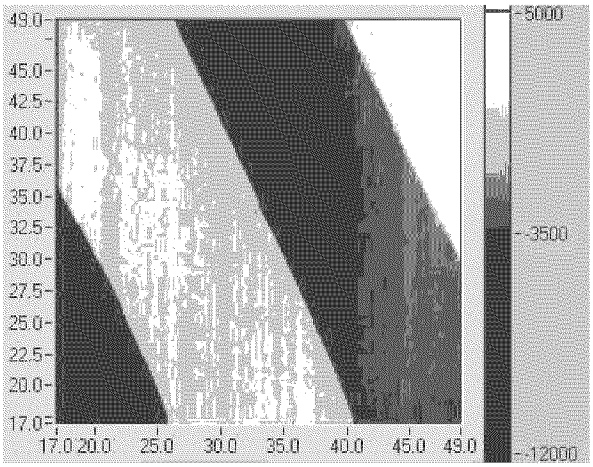

Figure 12 SFM piezoresponse image of the periodical domain pattern in CLN.

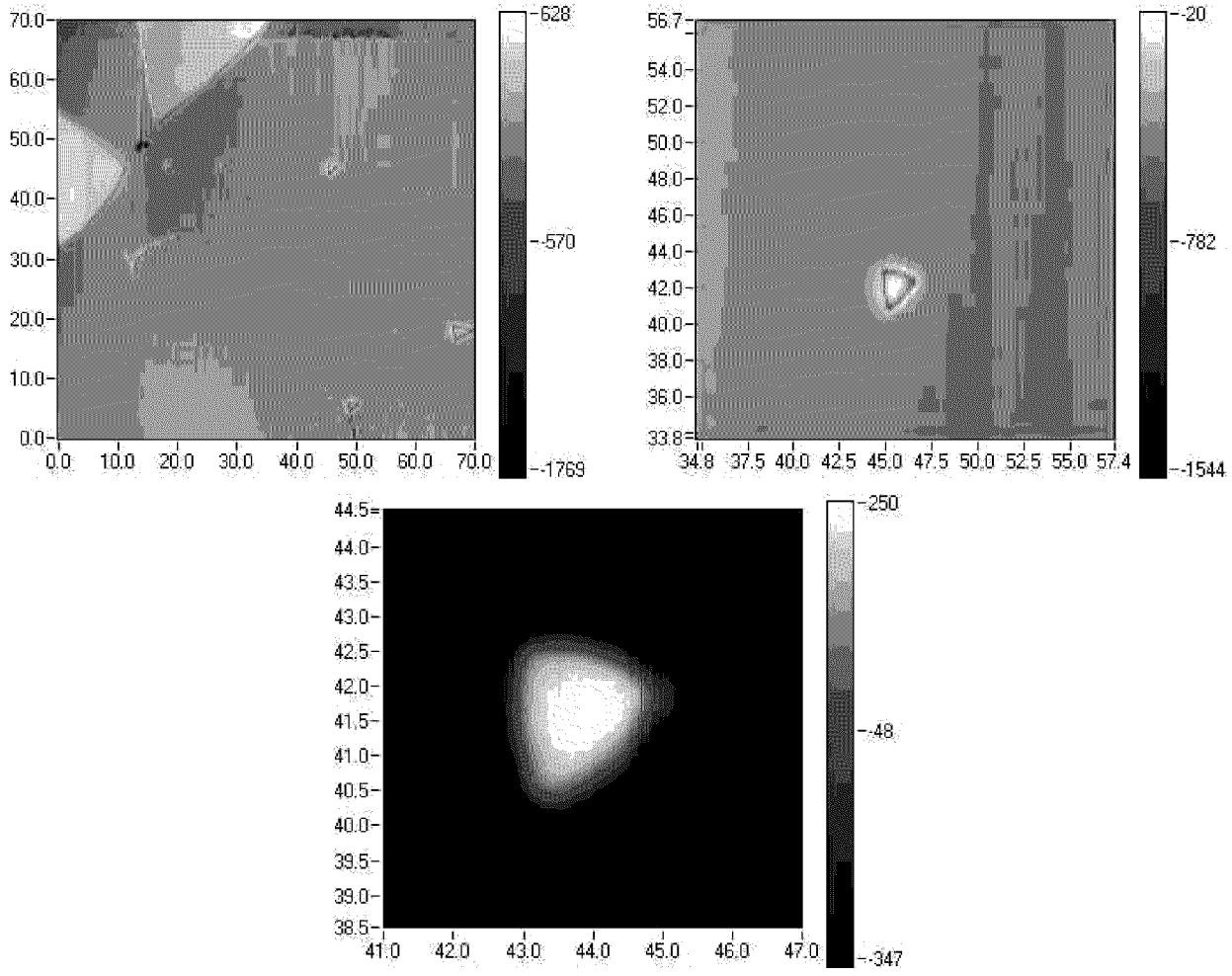

Figure 13 SFM piezoresponse image of the individual domains in CLT.

The method demonstrates the good contrast and high enough spatial resolution for nondestructive investigation of the nanoscale domain patterns in near future.

4 Main approach to the domain structure evolution

Our approach to kinetics of domain patterning in the bulk ferroelectrics is based on the assumption of key role of screening effect [13]. It is clear, that switching from the single- domain state is achieved through nucleation and growth of reversal domains [12]. The polar component of local electric field $\mathbf{E_Z}$ at the nucleation sites and domain walls governs both nucleation and growth respectively [12,13]. The spatial distribution of the local field $\mathbf{E_Z}(r,t)$ is determined by the sum of z components of: 1) external field $\mathbf{E_{ex}}(r)$ produced by the voltage applied to the electrodes, 2) the depolarization field $\mathbf{E_{dep}}(r,t)$ produced by bound charges of instantaneous domain pattern, and 3) screening fields of two types: the external one $\mathbf{E_{escr}}(r,t)$ due to the charge redistribution at the electrodes and the bulk one $\mathbf{E_{bscr}}(r,t)$ which compensates the residual depolarization field and external field by various bulk mechanisms [12,21,22].

$$E_Z(r,t) = \left[E_{ex}(r) - \left(E_{dep}(r,t) - E_{escr}(r,t)\right)\right] - E_{bscr}(r,t) \qquad (3)$$

The depolarization field slows the domain growth while the screening processes reduce its influence. It is important to keep in mind that without bulk screening even after complete external screening the bulk residual depolarization field $\mathbf{E_{dr}}(r)$ remains due to the surface dielectric gap existing in any ferroelectric [12,22].

$$E_{dr}(r) = E_{dep}(r) - E_{escr}(r) \neq 0 \qquad (4)$$

For an infinite single-domain ferroelectric capacitor

$$E_{dr}(r) = \frac{2LP_S}{\varepsilon_L \varepsilon_o d} \qquad (5)$$

where **L** - thickness of dielectric gap, **d** - thickness of the sample,

$\mathbf{P_S}$ - spontaneous polarization, $\boldsymbol{\varepsilon_L}$ - dielectric permittivity of the gap.

This residual field can be screened by the charge redistribution in the bulk and aligning of polar defects [21,22]. These processes are relatively slow ($\tau \sim 10^{-1}$-10^{5} s) [12] and usually obtained retardation of the bulk screening leads to various memory effects [13]. For example, after fast enough decreasing of the external field, the spontaneous backswitching process can partially or completely reconstruct the initial domain state. This process is determined by action of partially screened residual backswitched field.

$$E_{bs}(r,t) = -\left[E_{dr}(r) + E_{bscr}(r,t)\right] \qquad (6)$$

It must be stressed that in the case of long enough duration of switching pulse and fast diminishing rate of external field at the end of pulse the bulk screening field $\mathbf{E_{bscr}}$ can be extremely high due to the bulk screening of external field. As a result just after fast removing of external voltage the backswitching field can sufficiently exceed the necessary value of driving field, thus, the high degree of nonequilibrium can be achieved. In the case of exponential behavior of bulk screening field the following expression can be written backswitching field just after removing of external field $\mathbf{\Delta t_{sp}}$.

$$E_{bscr}(r, \Delta t_{sp}) = \left[1 - \exp\left(-\frac{\Delta t_{sp}}{\tau}\right)\right] \cdot [E_{ex}(r) - E_{dr}(r)] \qquad (7)$$

5 Switching in uniform field in congruent lithium niobate and lithium tantalate

We have investigated the polarization reversal in CLN and CLT using real-time observation of the domain evolution and simultaneous recording of the switching current data with its subsequent mathematical treatment.

5.1 Switching current data

The investigated 200-μm-thick plates of CLT and CLN cut normal to polar axe were switched by rectangular field pulses using circular liquid-electrolyte electrodes (LiCl) on both surfaces. The total switched area (1-mm-diameter) was visualized using polarized microscope and the sequence of instantaneous domain patterns was recorded on video during switching. Simultaneously the switching current was recorded in conventional manner (by Merz technique) [23]. The comparison of obtained current data and domain patterns allowed to extract the unique complete information about the domain structure evolution and to propose the main mechanisms of the domain wall motion.

The domain switching in CLT and CLN demonstrates essential "unipolarity": the threshold fields for switching from the initial domain state ("poling") and reversal switching ("repoling") are sufficiently different. The degree of unipolarity can be characterized by the value of bias field

$$E_b = 0.5\,(E_c^+ + E_c^-) \qquad (8)$$

The bias field in CLT is much larger than in CLN. The values of parameters extracted from the direct optical observation of the domain kinetics are presented in Table 2.

The switching process in CLT displays an essential "formation" effect, which manifest itself in decreasing of the switching time (Fig. 14) and threshold field (Table 2) after several switching cycles in the same conditions. It must be stressed that the bias field does not change while the threshold field decreases essentially.

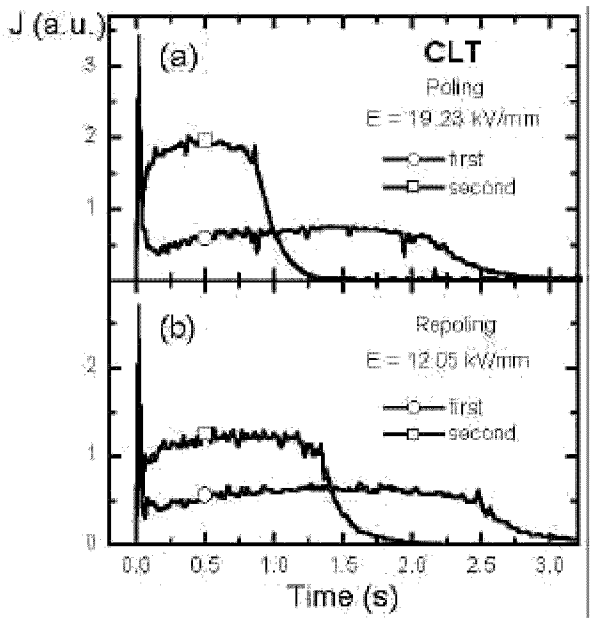

Figure 14 Effect of formation in CLT. Change of the switching currents for two sequent switching cycles.

Table 2. Threshold and bias internal fields for congruent and stoichiometric LN and LT.

	Threshold field, kV/mm		Bias internal field, kV/mm
	Poling	Repoling	
CLN	20.6	15.3	2.65
CLT (first switching cycle)	20.6	11.3	4.65
CLT (after cyclic switching)	19.2	10.0	4.60
VTE LT (T = 1220 ^{o}C)	1.23	1.15	0.08
SLT	2.0	1.7	0.15

The switching current pulse changes essentially with increasing of applied voltage (Fig. 15). Moreover at any voltage one can see the current noise (Barkhausen pulses) which can be related with jump-like motion of the domain walls [24,25].

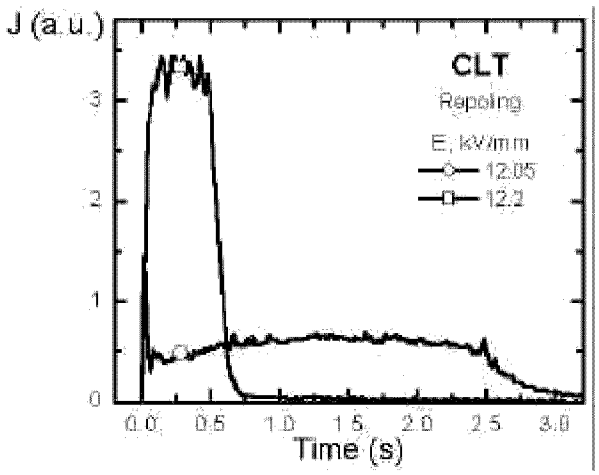

Figure 15 Switching currents measured for different voltages in CLT.

5.2 Domain shape during switching in lithium tantalate

We have investigated in details the shape of the domains arising during switching in CLT samples switched in uniform field applied by liquid electrolyte electrodes. The domain patterns revealed by etching on polar surface and cross-sections were visualized by optical microscope. It was shown that domain shape at different stages of cyclic switching varies essentially from ideal triangles (Fig. 16a) to triangles with round corners (Fig. 16b) and irregular hexagons. Moreover the unusual trefoil shape is observed also (Fig. 16d,e,f).

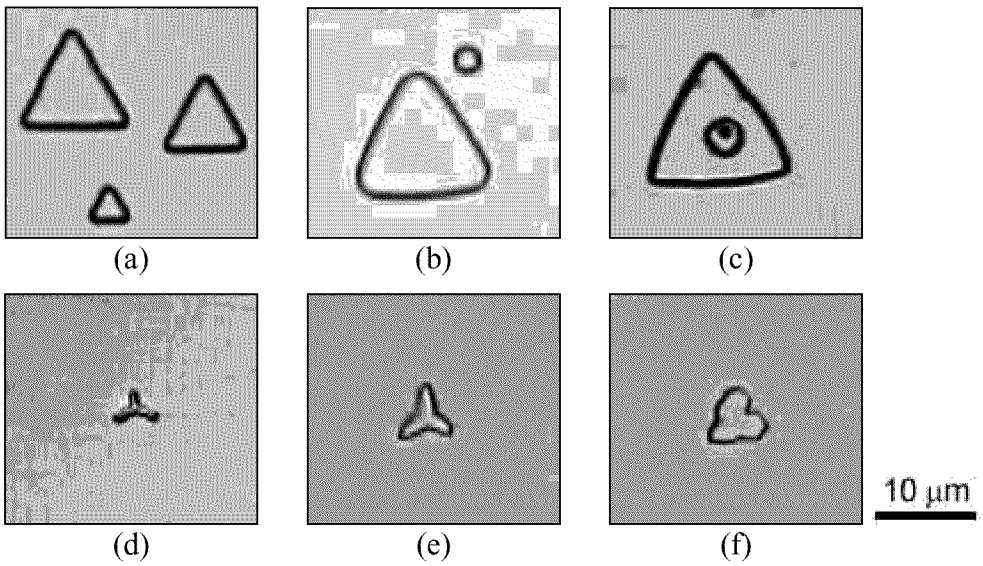

Figure 16 Variants of the domain shape in CLT. Domain patterns revealed by etching and visualized by optical microscope.

Such evolution of the domain shape can be explained if we take into account the evolution of the domain growth during cyclic switching. The domains arising in single-domain state demonstrate the regular shape, which is determined by the crystal symmetry. The evolution of such domains during backward switching is more complicated and its shape depends also on

prehistory due to memory effect, which is generated by the spatially nonuniform bulk screening field. The variation of step's position at the wall and velocity of their propagation along the wall leads to formation of several unusual shapes considered above.

The special case of domain evolution during backward switching is presented in Figure 16c. The surface defect plays a role of nucleation site during both switching and backward switching. As a result during backward switching the new domain arises and grows in the center and the shape of triangle domain changes due to specific of step propagation in the corners of switched domain. Such mechanism leads to formation of the domain triangles with round corners (Fig. 16b).

We have investigated also the domain forward growth through the sample using the patterns visualized on slightly tilted cross-sections (Fig. 17). It was shown that growing domains have a shape of triangular pyramid and finally become the triangular prism with vertical neutral domain walls (Fig. 17a). The tilted cross-sections show the details of domain face's shape and demonstrate in many cases their essential irregularities (Fig. 17b,c).

It is important to point out that in all investigated samples domains nucleate at the surface. Such results refute the recent confirmation of Gopalan [26] about domain nucleation in the bulk of CLT. Our detail observations show that his patterns were observed at the cross-sections with uncontrolled deviations of orientation.

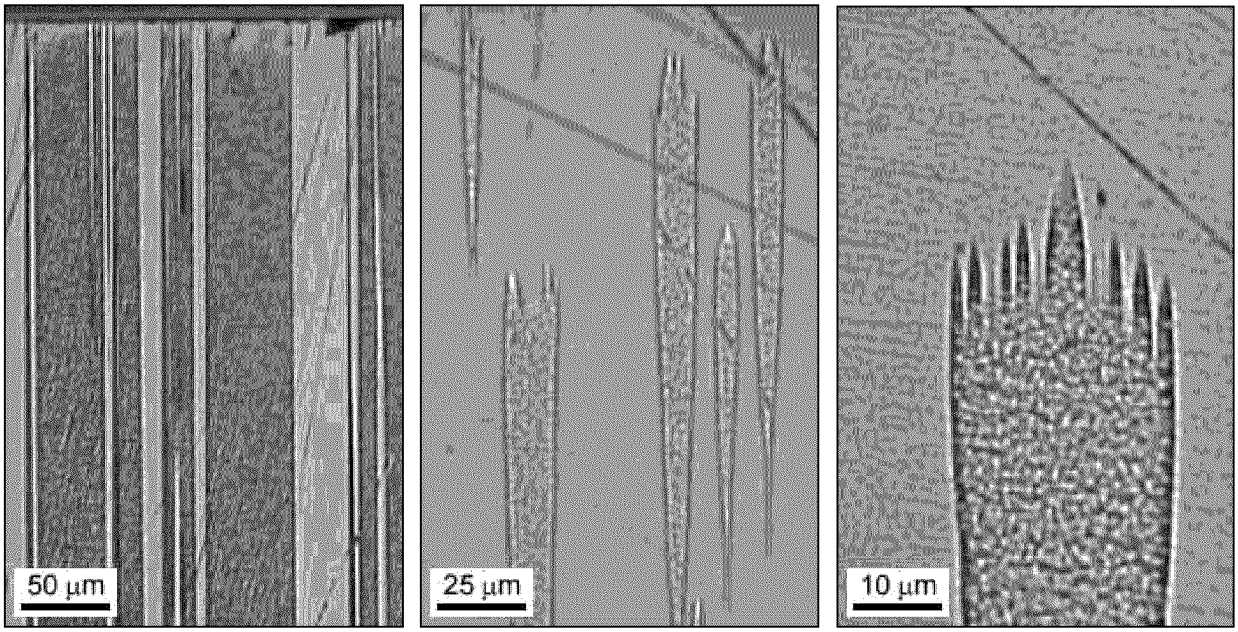

Figure 17 Domain patterns in CLT on slightly tilted cross-sections. Domain patterns revealed by etching and visualized by optical microscope

5.3 In situ observation of the domain kinetics in lithium niobate

The direct observation of the domain kinetics during switching has been used for detail studying of the domain structure evolution in CLN (Fig. 18). We have obtained the hexagon domain shape. One can see the pronounce irregularities in wall propagation and its interaction with individual arisen domains. Moreover the preferential orientation of the walls is brightly demonstrated from the beginning to the end of switching.

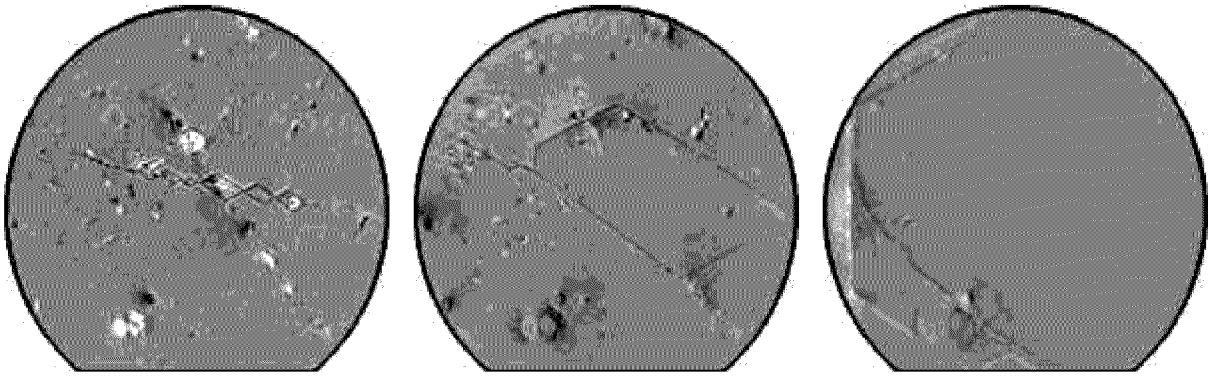

(a) (b) (c)

Figure 18 Evolution of the domain structure during repoling in uniform external field in CLN. Diameter of the poling area 1 mm, E = 15.3 kV/mm.

The typical evolution of the domain structure in CLN is the nucleation along the edges of electrodes and propagation of the formed domain walls to the center of the switching area. Another scenario was obtained in the samples with surface defects. In the case shown at Figure 18 we choose the special crystal area with small scratch in the center. Such artificial nucleation sites leads to start of switching in the center and domain growth to the boundaries of the switched area. The domain shape is far from the regular hexagons but all domain walls are oriented along **Y** directions. Any local deviation from the allowed crystallographic orientations rapidly disappears. The domain growth is usually connected with the propagation of microscale domain steps along the wall (Fig. 19).

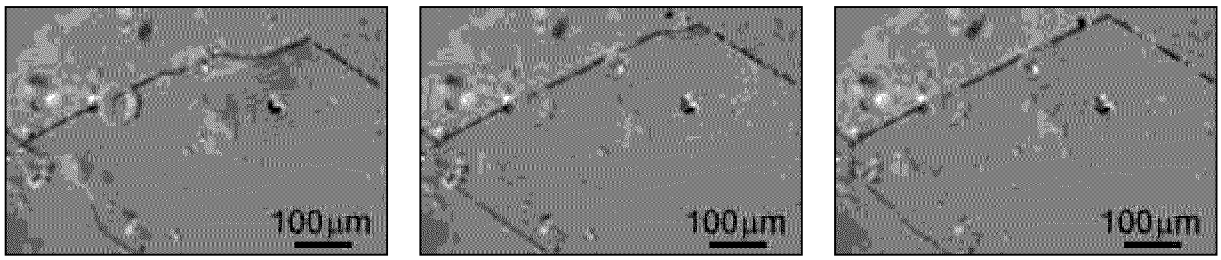

(a) (b) (c)

Figure 19 Layer-by-layer growth through step propagation along the wall during repoling in uniform external field in CLN. Time interval between the sequent frames 2 s, E = 15.3 kV/mm.

The fastest step of the domain evolution is connected with transformation from concave domain shape (forming as a result of merging) to the regular convex one. The typical scenario of the event when fast the big domain "gulp" the small one is demonstrated at Figure 20. Moreover it must be stressed that the prints of the domain wall are observed after wall shift (Fig. 20). The prints appear only at the places where the wall was staying for long enough time (more than second). These prints gradually disappear in time interval about one second. The lifetime of the print is proportional to the time of wall staying in stable position.

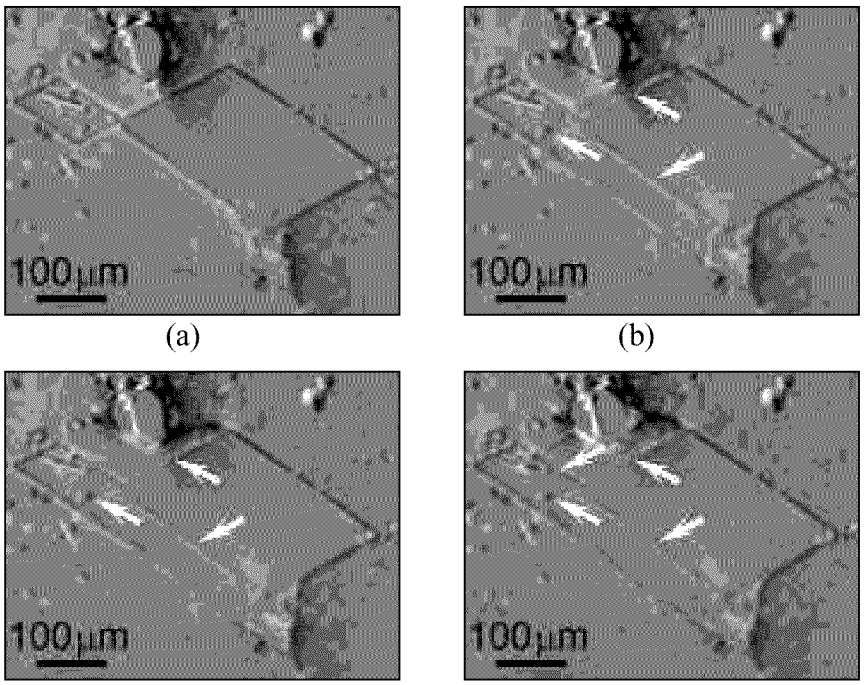

Figure 20 "Gulping" during repoling in uniform external field in CLN. Arrows indicate the prints of the domain walls. Time interval between the sequent frames 40 ms, E = 15.3 kV/mm.

In situ domain observation opens the possibility to measure directly the average sideways wall motion velocity and its field dependence (Fig. 21). It was shown that experimental data measured in wide range of the velocities can be fitted by conventional exponential law

$$V(E) = V_{\infty} \exp[E_{ac}/(E - E_{th})] \qquad (9)$$

The main parameters of approximation are presented in Table 3.

Table 3. Parameters of voltage dependence of the average sideways domain wall motion velocity in CLN

	Poling	Repoling
Activation field ($\mathbf{E_{ac}}$), kV/mm	47.2	13.8
Threshold field ($\mathbf{E_{th}}$), kV/mm	17.8	14.0

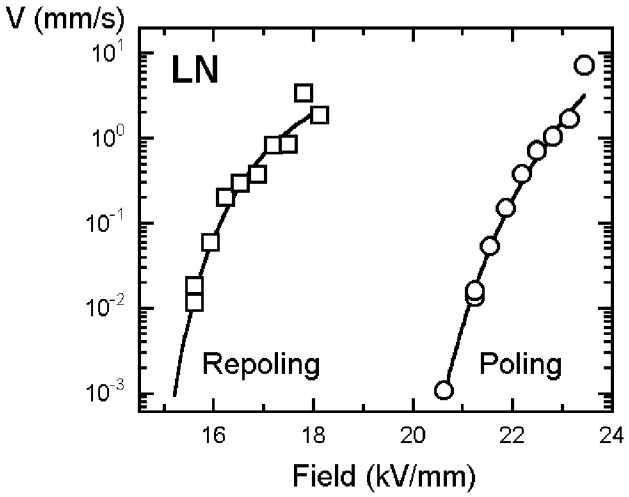

Figure 21 Field dependence of the average velocity of the domain wall motion in CLN. Experimental points are fitted by Equation (9).

5.4 In situ observation of the domain kinetics in lithium tantalate

5.4.1 Domain evolution

The main features of the domain evolution in CLT are similar to that in CLN. But the nucleation along the edges of electrodes in CLT is negligible and the density of arising domains is about 1000 mm^{-2} (Fig. 22a). In this case the shape of growing domains is more irregular due to permanent merging of the moving walls with individual domains (Fig. 23). The clear tendency to reconstruct the regular shape of domains after merging is also obtained.

(a) (b) (c)

Figure 22 Evolution of the domain structure during poling in uniform external field in CLT. Diameter of the poling area 1 mm, E = 19.2 kV/mm.

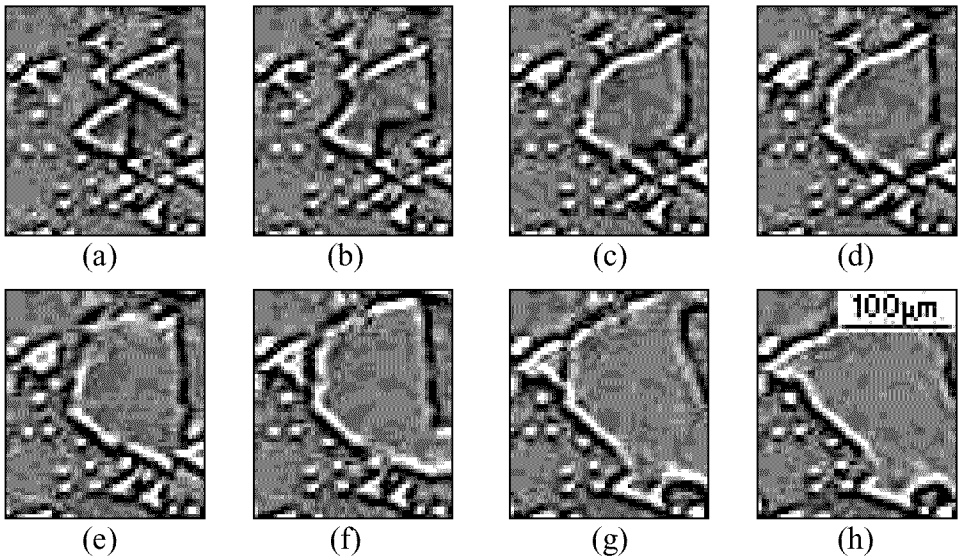

Figure 23 Jump-like motion of the domain wall in CLT. Time interval between the sequent frames 40 ms, E = 19.2 kV/mm.

The significant difference in domain evolution scenarios between CLT and CLN is connected with coexistence of "fast-growing" and "slow-growing" domains in CLT (Fig. 24). The small slow-growing domains appear at the very beginning of the switching process and then enlarge extremely slow. The fast-growing domains are formed as a result of merging of the closest neighbor small domains. Sideways wall motion of fast-growing domain represents the sequence of step generation acts through wall merging with slow-growing domains. The arisen steps propagate rapidly along the wall (Fig. 24).

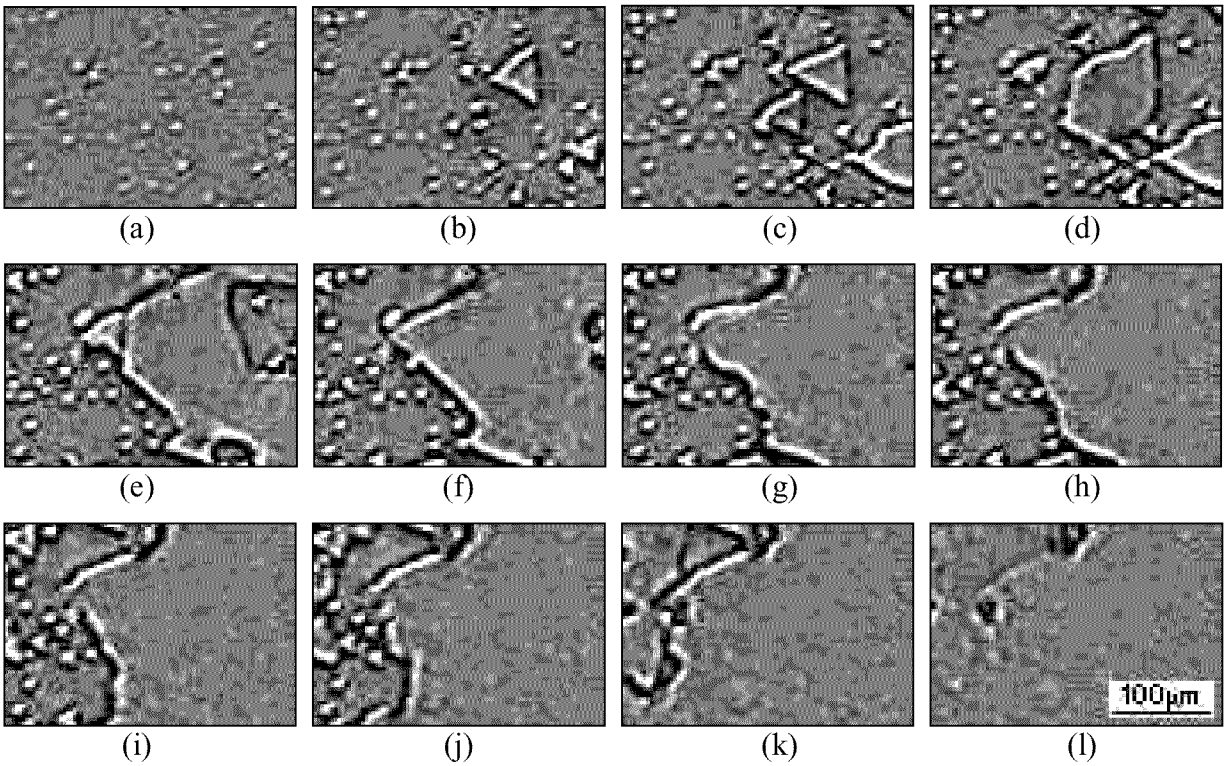

Figure 24 Domain wall motion by merging with slow-growing domains in CLT. Time interval between the sequent frames 160 ms, E = 19.2 kV/mm.

Such behavior can be explained by the following mechanism. The slow-growing domains appear at nucleation sites defined by surface defects and nonuniform distribution of the bias internal (bulk screening) field. Their growth velocity is decreased with size increasing due to slow screening of depolarization field. Thus they can merge only if the distance between the nucleation sites is short enough (about 10 μm). The subsequent continuous motion of domain wall by step propagation can be obtained only if the wall length is long enough to "find" the isolated domains, which are the only source of the steps. It is clear that the observed jump-like wall motion should lead to switching current noise (Barkhausen jumps) (Fig. 25).

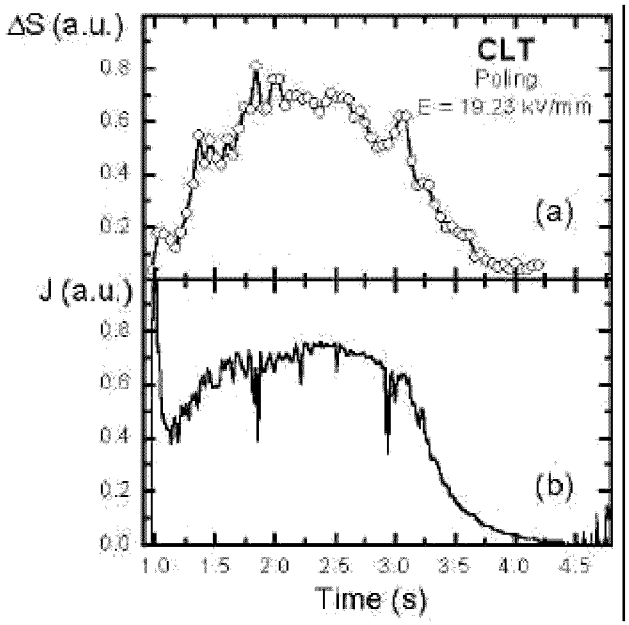

Figure 25 Comparison of the time dependencies of the switching current **J** and the derivative on time of the switched area **ΔS**, calculated by image processing of the instantaneous domain patterns in CLT.

It must be pointed out that the domain kinetics differs qualitatively for first poling (from single-domain state) (Fig. 26) and for any subsequent poling or repoling (Fig. 27). The nucleation density for the first poling is much lower and the domain shape is more regular then for subsequent switching. The obtained results can be connected with two effects. First, the bulk screening changes the initial uniform distribution of threshold field according to domain kinetics during first switching. Second, supposed effect of arising of needle-like backswitched domains just following the moving wall. During subsequent switching growth of these domains defines the arising of individual domains and also the wall propagation.

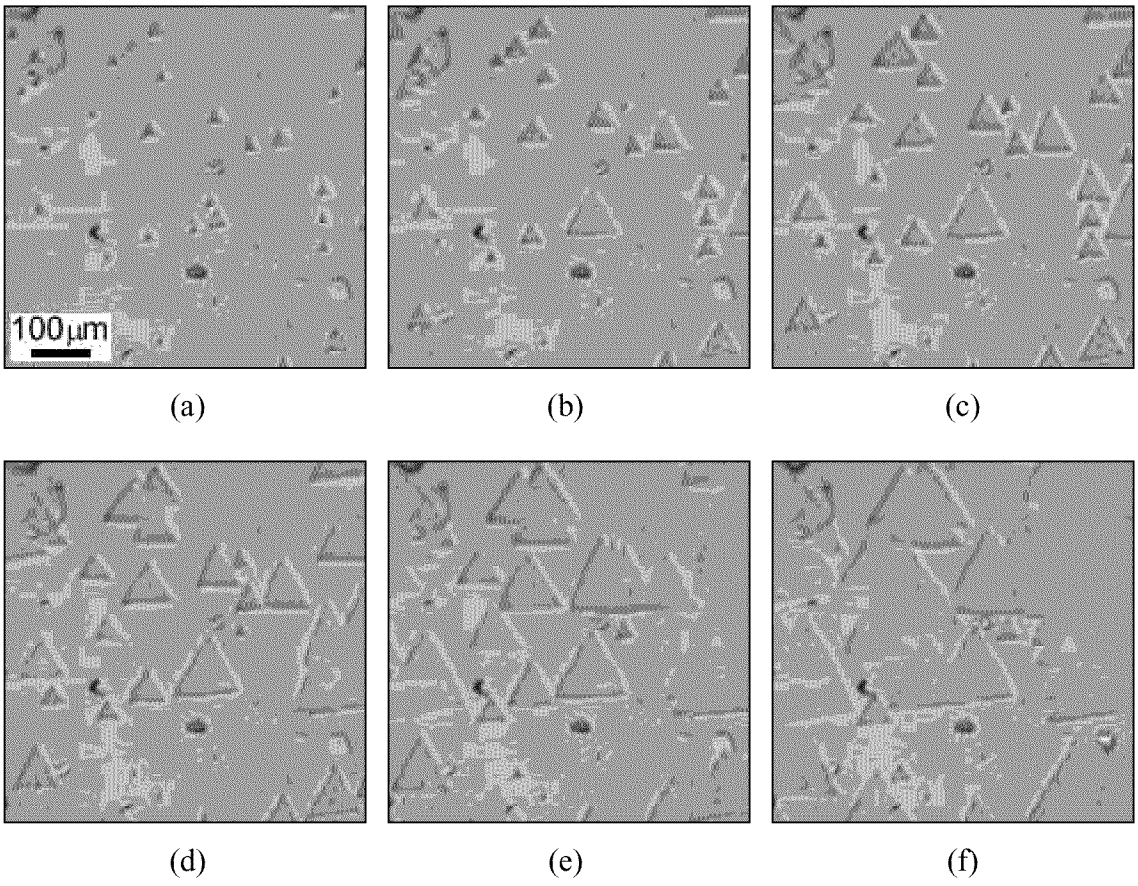

Figure 26 Evolution of the domain structure during first poling in CLT. E = 22.5 kV/mm.

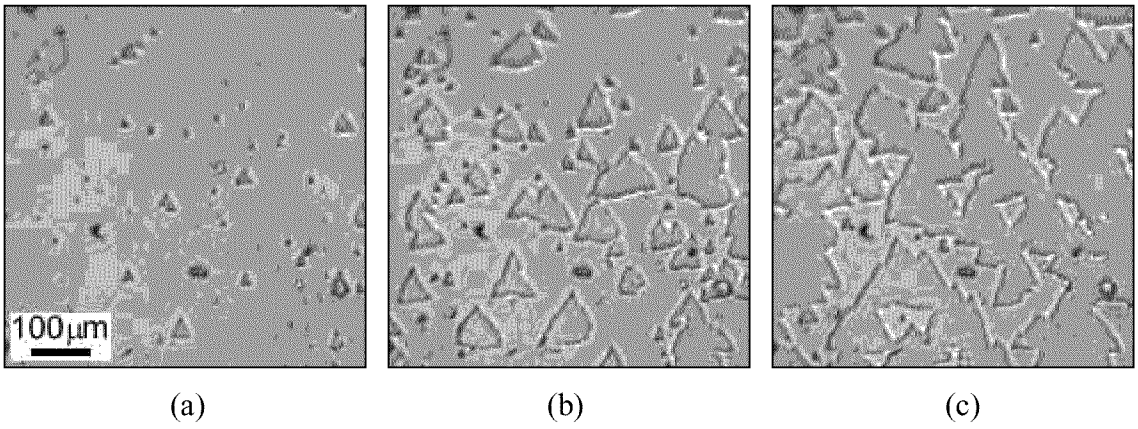

Figure 27 Evolution of the domain structure during subsequent poling in CLT. E = 22.5 kV/mm.

Moreover we demonstrate for subsequent switching cycles in low field value (just above the threshold) the unusual domain kinetics presenting growth of irregular-shape domains and formation of the maze domain structure (Fig. 28). Such behavior is consistent with the above consideration and can be determined by inhomogeneous spatial distribution of threshold fields.

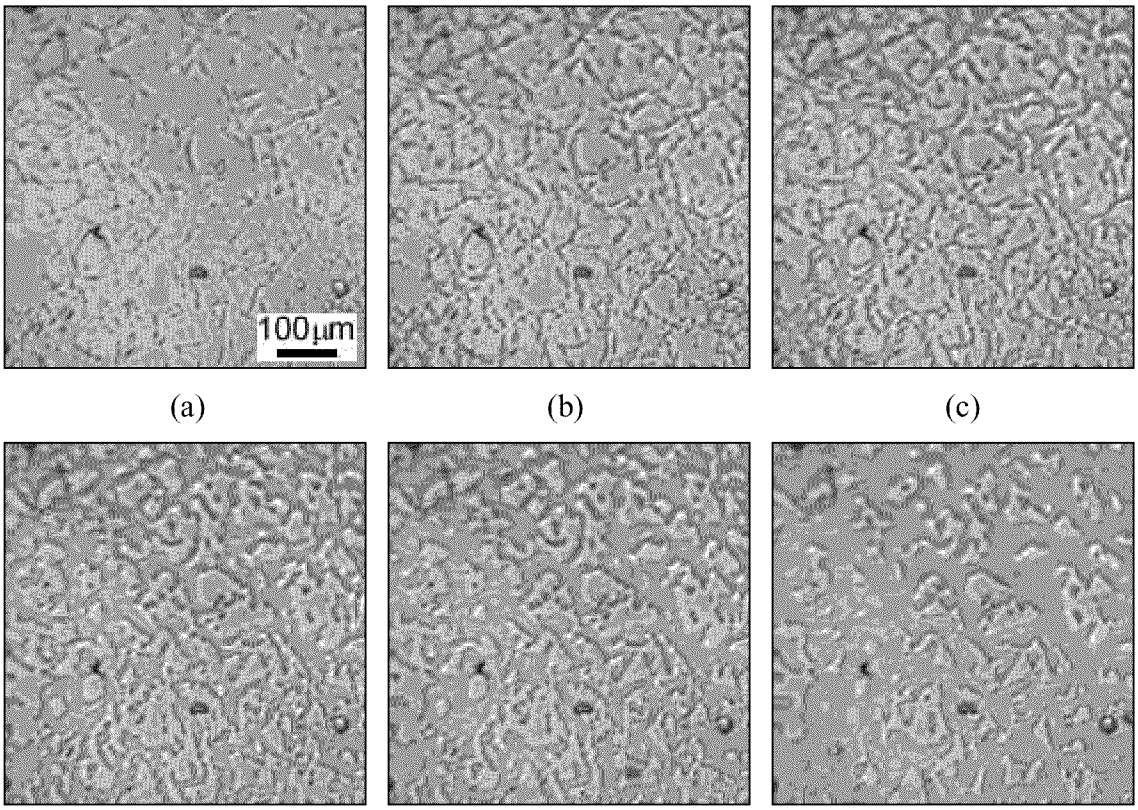

Figure 28 Evolution of the domain structure during repoling in low field in CLT. E = 15 kV/mm.

5.4.2 "Optical" switching current

The image processing of the sequence of instantaneous domain patterns allows to obtain the time dependence of the switched area derivative **ΔS**, which is proportional to the switching current **I**. The comparison of the time dependencies demonstrates their qualitative similarity (Fig. 25) thus proves the basis of mathematical treatment of the switching current data. It is possible to obtain the "optical" switching current at different parts of the sample. Such analysis shows that different areas of the sample demonstrate two types of qualitatively different behaviors (Fig. 29). Some places (with high enough density of the nuclei) show the conventional kinetics ("nucleation & growth") with typical switching current shape for β-process (Fig. 29a) [27]. The data have been fitted by Kolmogorov-Avrami formula [27,28]. The spatially nonuniform nucleation leads to existence of the sample areas without any fast-growing domains due to large distance between the nucleation sites. These regions switch by propagation of the domain walls formed in the neighboring regions. The current data for such behavior can be fitted by our original modification of K-A formula for spatially nonuniform nucleation with catastrophe at the moment when the walls reach the boundary of the switched area (Fig. 29b) [29]. Thus the optical and conventional

switching current data can be fitted by the formula consisting of two inputs considered above (Fig. 30a,c).

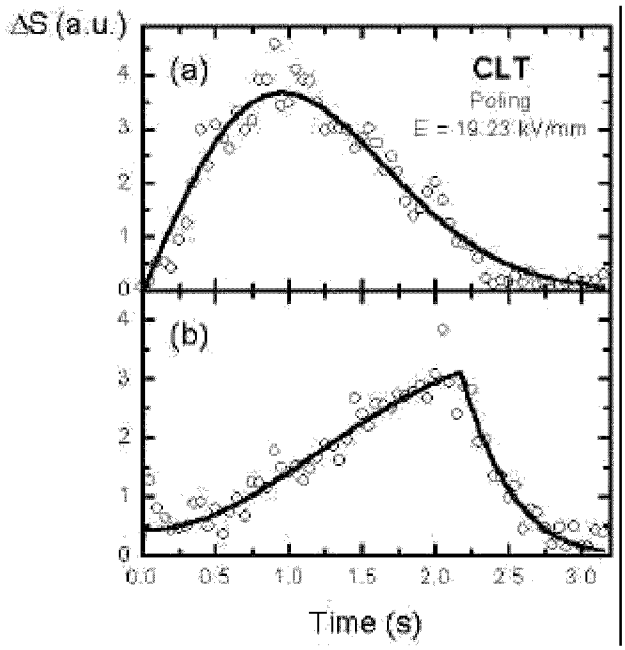

Figure 29 Optical switching current **ΔS** in different region types switched by (a) nucleation and growth and (b) propagation of the domain walls formed in the neighboring region in CLT fitted by theoretical equations.

It is clear that the number of current jumps should be observed in both cases due to irregular reconstruction of the walls of growing domains (Fig. 30b,d). Therefore the analysis of the current data can carry out the details of fast domain evolution.

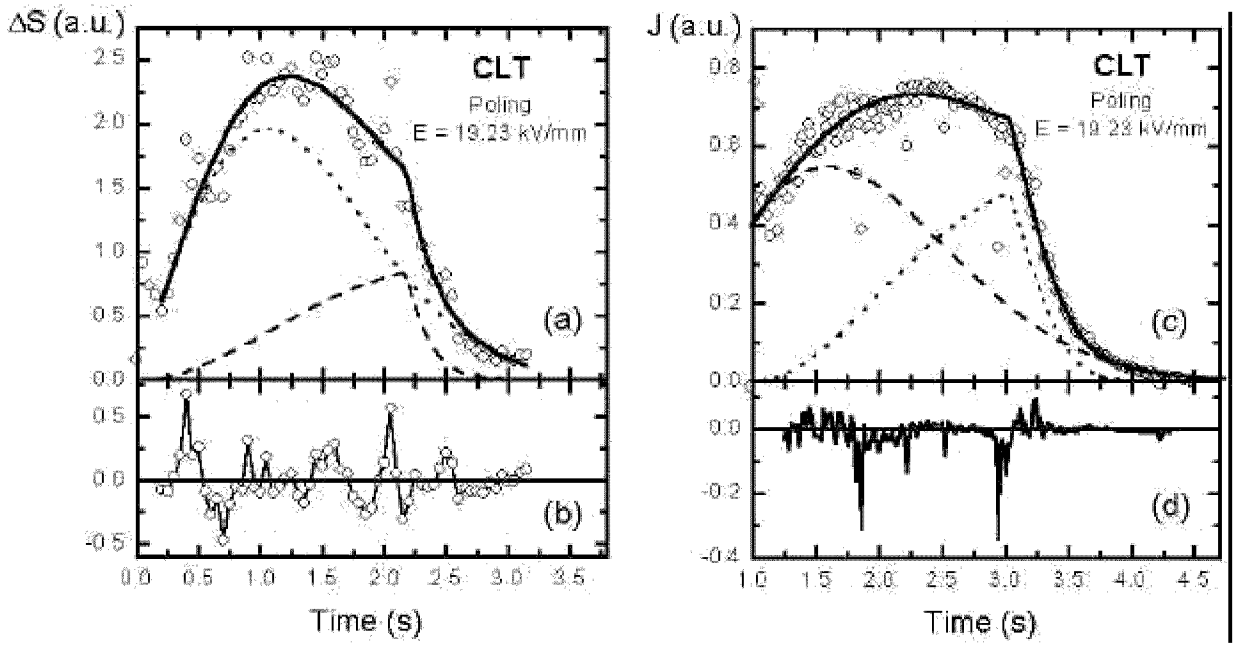

Figure 30 Time dependencies of the switching currents in CLT (fitted by theoretical equations) obtained by (a) "optical" **ΔS(t)** and (c) "conventional" **J(t)** methods and (b) and (d) - current deviations from the best-fit curves.

5.4.3 Simulation of the original domain kinetics observed in congruent lithium tantalate

We have done the preliminary computer simulations of the observed mechanism of domain evolution through the nucleation of slow-growing domains and the fast domain growth by propagation of the steps generated as a result of domain merging. Several instantaneous patterns of domain evolution simulated in 100x100 matrix with 1500 randomly distributed initial nuclei are presented in Figure 31.

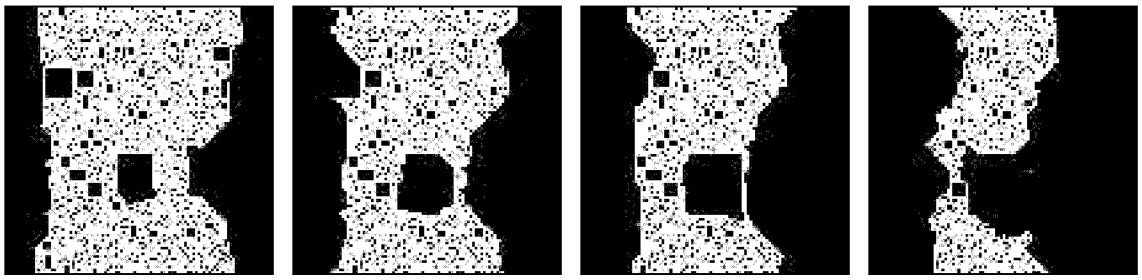

(a) (b) (c) (d)

Figure 31 Simulated instantaneous domain patterns.

The initial domain configuration in considered case contains two domain walls at the left and right boundaries of "switched area". The obtained current data (Fig. 32) is quite similar to optical and conventional experimental data (Fig. 25). Therefore the proposed mechanism of domain evolution is qualitatively confirmed. Further simulations will be done for quantitative confirmation of the proposed methods of switching current treatment.

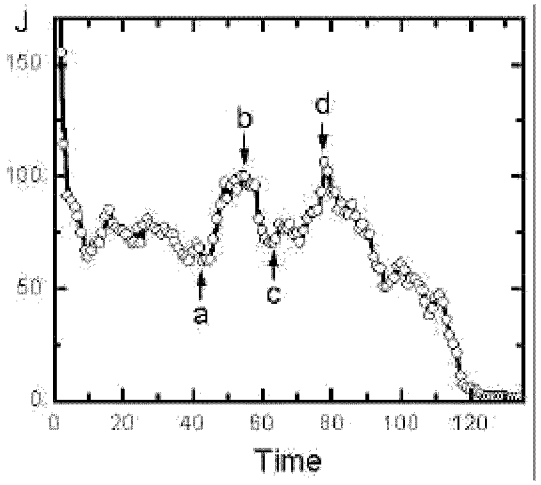

Figure 32 Simulated switching current corresponding to the patterns at Figure 31.

We have simulated also the limiting case when the arisen nuclei never grow and calculated the critical nuclei concentrations needed for propagation of plane wall (with given length) on given distance. As a result we present the dependence of the probability of domain wall propagation on the wall length for given shift and fraction of the initial nuclei (Fig. 33).

Moreover the dependence of the wall length needed for its propagation (with given probability and fixed shift) on the fraction of the nuclei area have been calculated (Fig. 34). The obtained results can be used for analysis of the critical local domain concentrations needed for arising of fast-growing domains and the minimal domain size (wall length) which guaranteed its continuous growth.

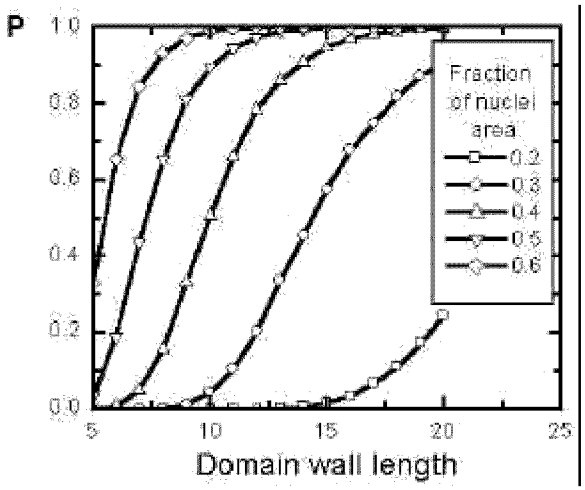

Figure 33 Dependence of the probability of domain wall propagation on the wall length for given shift ($\Delta x = 100$) and fraction of the initial nuclei. Results of computer simulation.

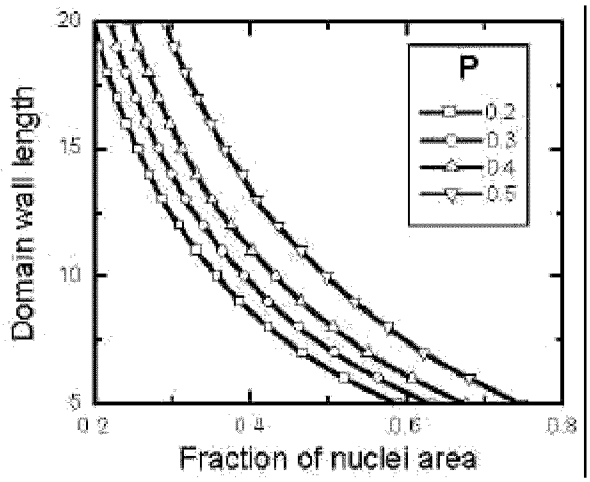

Figure 34 Dependence of the wall length needed for its propagation with given probability and given shift ($\Delta x = 100$) on the fraction of the nuclei area. Results of computer simulation.

6 Polarization reversal in stoichiometric lithium tantalate

6.1 Domain structure and switching in Vapor Transport Equilibration lithium tantalate

We have investigated static as-grown domain structure and switching parameters in the set of VTE LT samples annealed at different temperatures from 1120 to 1370^{O}C.

6.1.1 As-grown domain structure with charged domain walls and twins

We have visualized as-grown domain structure at the polished cross-sections using optical microscope in reflected mode. The samples have been etched for 30 – 50 min in hydrofluoric acid. It was shown that all structures formed as a result of phase transition without any external field contain the charged domain walls (Fig. 35) and twins (Fig. 36).

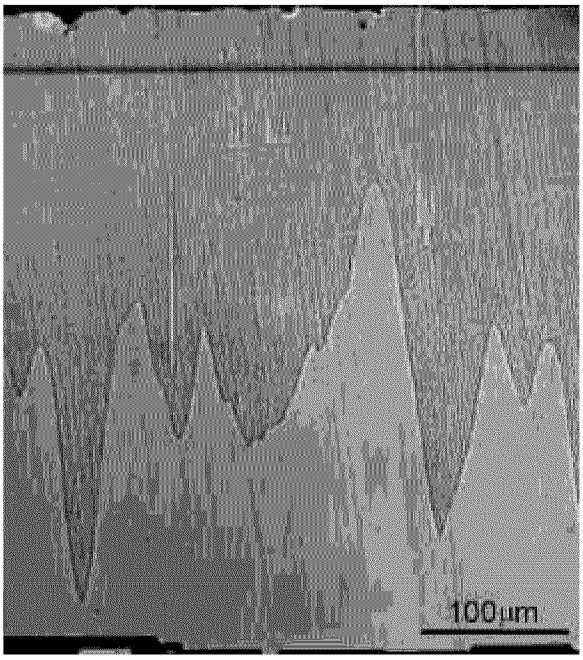

Figure 35 Charged domain walls in VTE LT annealed at 1220^{O}C. **Y** view. Domain patterns revealed by etching and visualized by optical microscope.

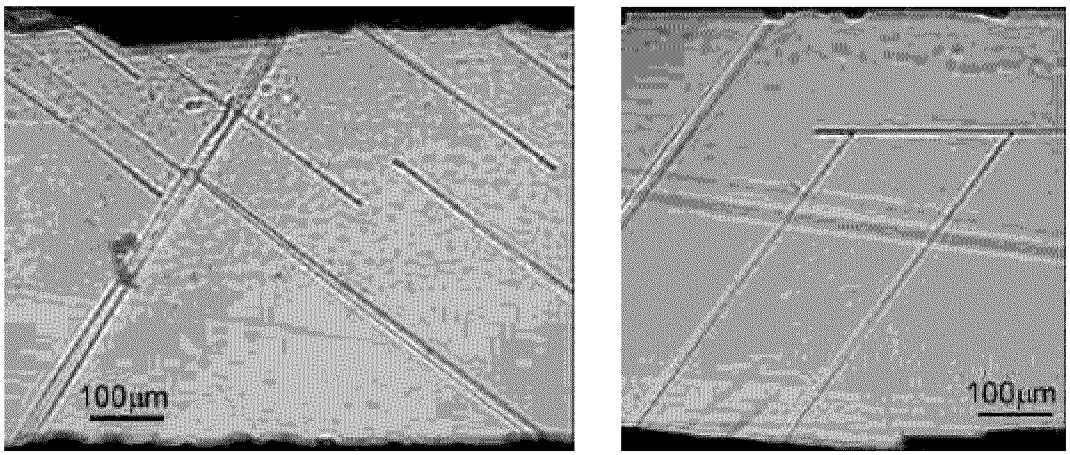

Figure 36 Twins in VTE LT annealed at 1170^{O}C. **Y** view. Twin patterns revealed by etching and visualized by optical microscope

The charged domain walls are usually irregular zig-zag shaped. Only in some samples annealed at low temperatures (about 1220^{O}C) the small domains with flat charged domain wall arise at the flat defects in the bulk (Fig. 35). Concentration of charged domain walls decreases

with increasing of annealing temperature. At the temperatures above 1300^{O}C we found only conventional domains without any charged walls (Fig. 37).

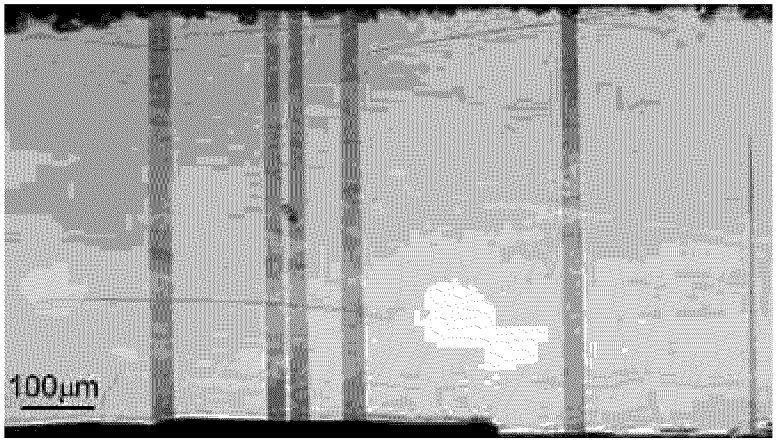

Figure 37 Domain structure with neutral walls in VTE LT annealed at 1320^{O}C. **Y** view. Domain patterns revealed by etching and visualized by optical microscope.

All samples annealed at low temperatures contain a number of plate-like twins strictly oriented along crystallographic directions (Fig. 36). The twins are clearly observed also in polarized light in transmitted mode (Fig. 38). The crossed twins usually generate the micro-scratches in the samples (Fig. 39). Arising of the twin structure indicates existence of the strong stresses in the bulk, which can be caused by concentration gradients in the annealed samples.

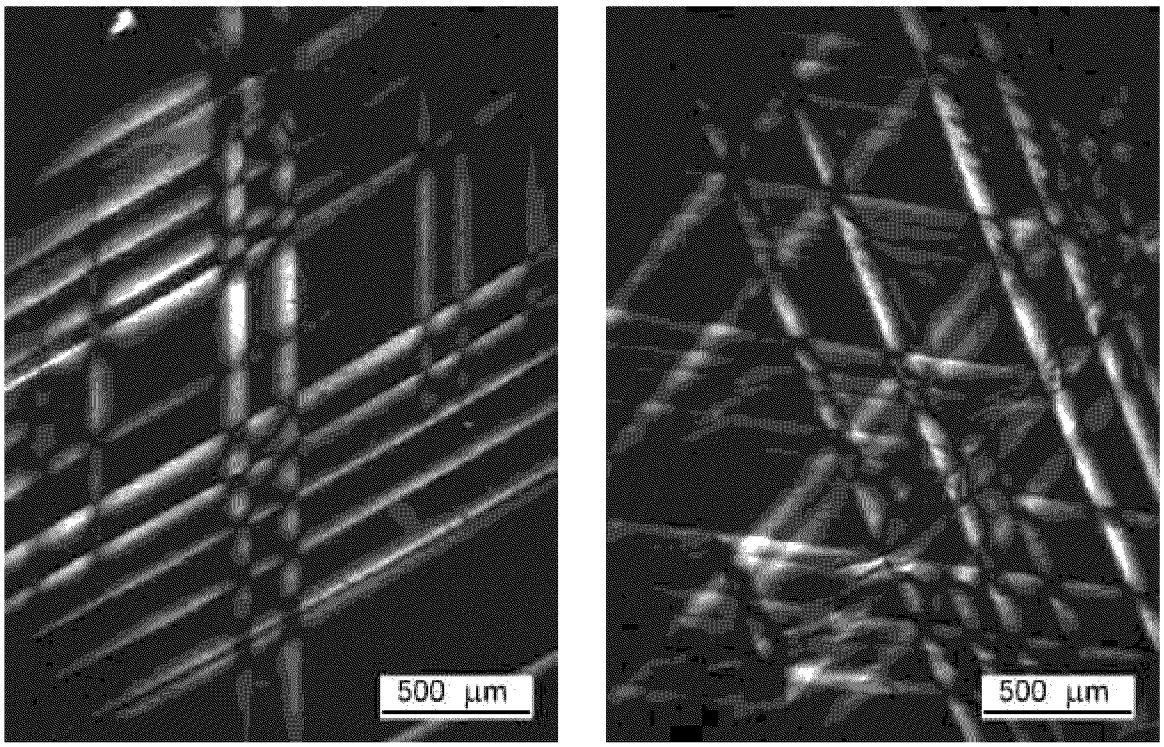

Figure 38 Twins in VTE LT annealed at 1170^{O}C. **Z** view. Twin patterns visualized by polarizing microscope in transmitted mode.

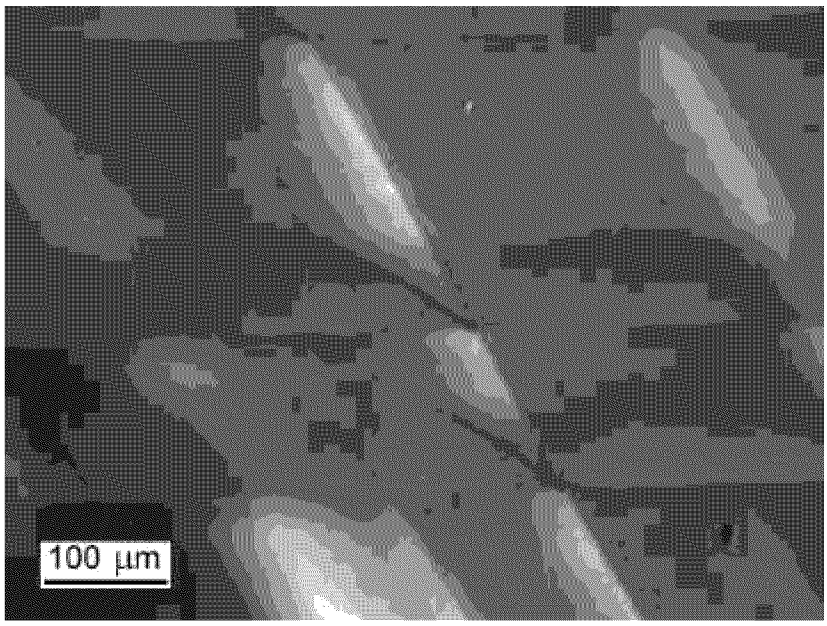

Figure 39 Twins and micro-scratches in VTE LT annealed at 1170^{O}C. **Z** view. Patterns visualized by polarizing microscope in transmitted mode.

It must be pointed out that we have observed a strong correlation between twins and domains (Fig. 40). The charged domain walls are frequently situated just at the twins' boundaries. Twins interrupt the domain growth from the surface through the bulk (Fig. 40a,b) or generate the domain growth in the bulk (Fig. 40c). As a result of twin-domain interaction the formed as-grown domain structure is very complicated and difficult for switching.

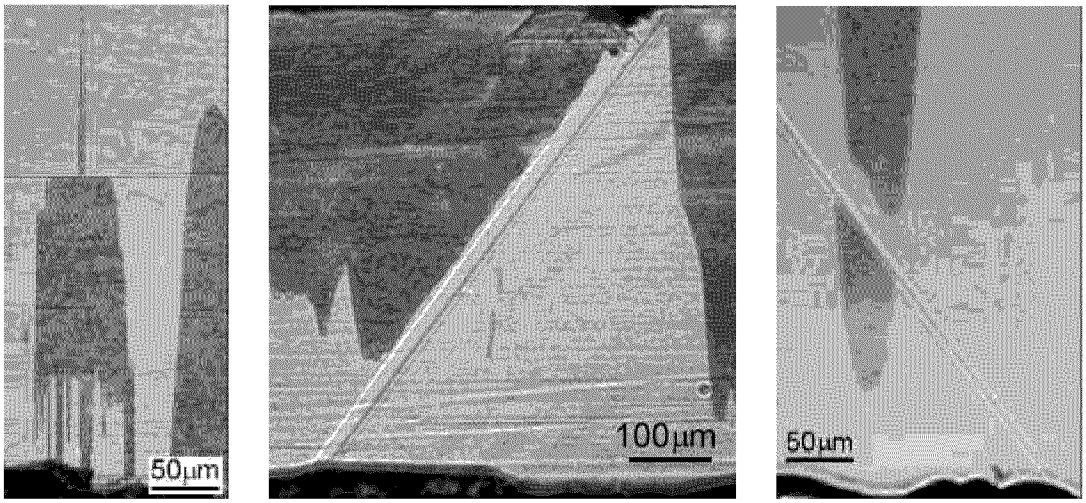

Figure 40 Domain-twin interaction in VTE LT annealed at (a) and (b) - 1120^{O}C, (c) - 1170 ^{O}C. **Y** view. Domain patterns revealed by etching and visualized by optical microscope.

The main tendencies in temperature dependencies of the twins and charged domain walls are summarized in Table 4. It is clear that the most uniform structures have been produced by treatment at the temperatures above 1320^{O}C.

Table 4. VTE LT samples annealed at different temperatures.

T, ^{o}C	Time, hours	Twins	Charged domain walls
1120	200	many in 3 directions	almost everywhere
1170	200	many in 3 directions	almost everywhere
1220	100	few "horizontal" only	almost everywhere
1320	100	few "horizontal" only	Few
1370	200	absent	almost absent

6.1.2 Switching currents and hysteresis loops

The main switching parameters were extracted from the current data measured in linear increasing field and rectangular field pulses for VTE LT samples annealed at 1220^{O}C. It was shown that the shape of switching current and parameters of the hysteresis loop varies from sample to sample due to the parameters of the local as-grown domain structure (Fig. 41). The averaged value of coercive field is about 1.2 kV/mm with bias about 0.1 kV/mm. Switching currents are always very noisy (Fig. 41a). Such behavior can be defined by the jump-like domain growth.

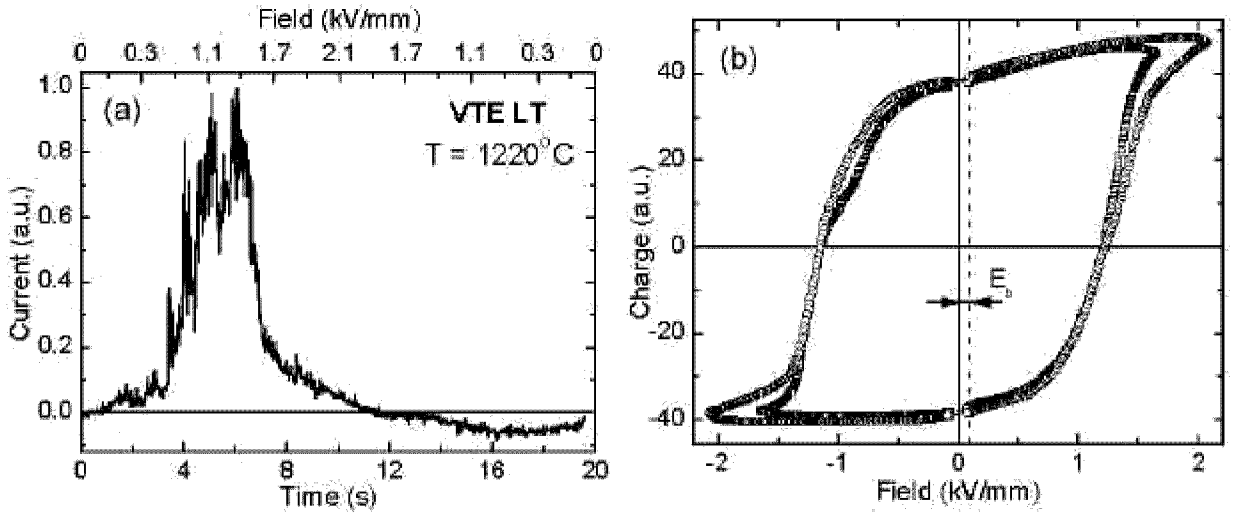

Figure 41 Switching current and hysteresis loop in VTE LT annealed at 1220^{O}C.
$\mathbf{E_c}$ = 1.2 kV/mm, $\mathbf{E_b}$ = 0.08 kV/mm.

The typical switching current obtained during switching in rectangular pulses is presented in Figure 42. After fast growth it becomes constant with growing noise amplitude. The decreasing part is practically noiseless.

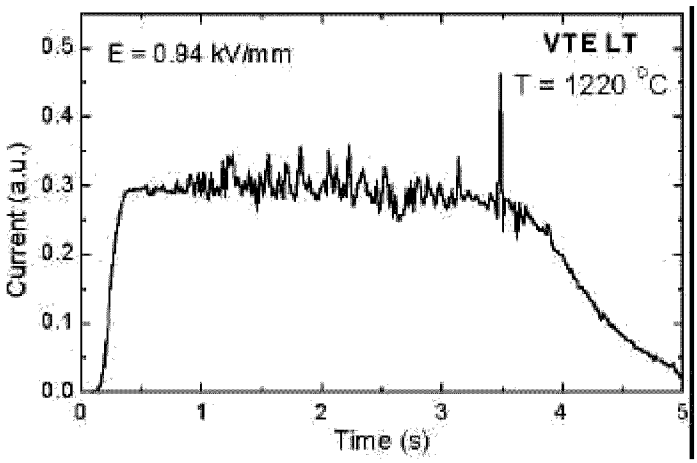

Figure 42 Switching current measured in rectangular field pulse in VTE LT.

In situ optical observation of domain evolution during switching shows the irregular maze-type micro-scale patterns with low contrast. Thus at the beginning existing domain walls move towards each other with constant velocity. Their jump-like motion leads to observed current noise. The walls' merging causes the current decrease. Such scenario of the domain evolution allows us to obtain the field dependence of the wall motion velocity in field range 0.8 – 3 kV/mm (Fig. 43). The obtained field dependence of the current pulse amplitude has been approximated by two linear dependencies with change of start fields and wall mobility at 1.7 kV/mm.

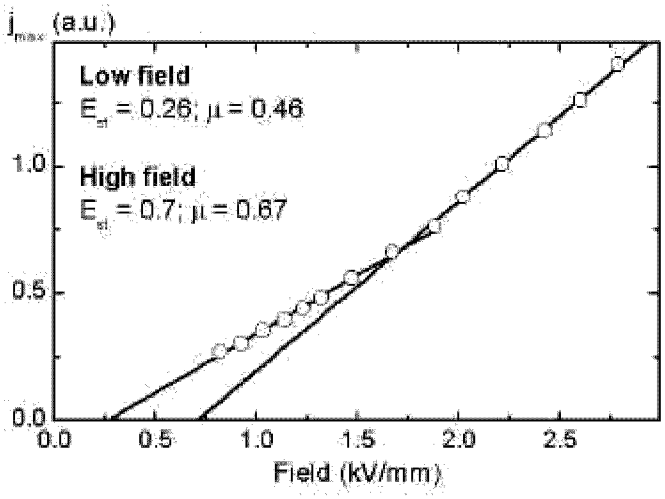

Figure 43 Field dependence of the current pulse amplitude in VTE LT annealed at 1220^{O}C.

6.2 Domains and switching currents in lithium tantalate grown by double crucible Czochralski method

Domain patterns observed in SLT samples by optical method without etching drastically differ from those obtained in CLT. The typical shape of SLT domains is just the same as in LN (compare Figures 4 and 5). Such hexagon shape is very convenient for periodical patterning as it permits to create the strip domains with ideal plane walls. Thus solve the problem existing in CLT.

In situ observation of domain kinetics in SLT demonstrates arising and growth of hexagons (Fig. 44). The peculiarities of domain evolution are very similar to those obtained in LN. The moving walls always keep strictly the allowed crystallographic orientations. The jump-like wall motion and "gulping" during domain merging are very typical.

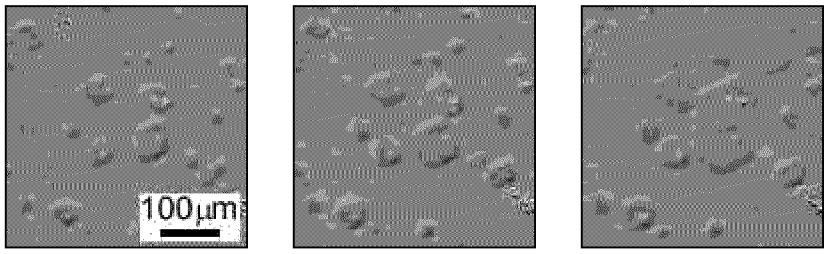

Figure 44 In situ observation of the domain kinetics in SLT during switching in linear increasing field.

The coercive field measured from hysteresis loop is about 1.85 kV/mm with bias about 0.15 kV/mm (Fig. 45b). The rectangular shape of the loop indicates absence of backswitching. The switching current measured in linear increasing field presents the series of short positive and negative pulses with duration about 10 ms (Fig. 45a).

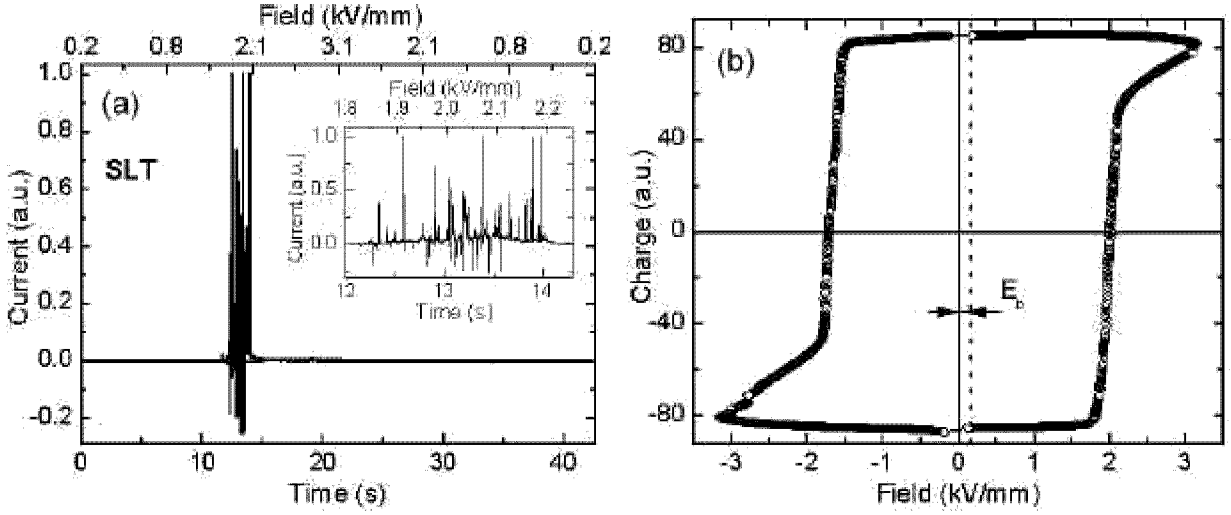

Figure 45 Switching current and hysteresis loop in SLT.

Such behavior is a bright demonstration of the jump-like domain evolution considered above. The negative current jumps can be explained by two mechanisms. First, after wall jump the backswitching occurs by formation of individual spike-like domains in just switched area. Second, the fast component of bulk screening process (by injection through intrinsic dielectric gap) leads to negative current of extra charge, which has provided the external screening. It must be stressed out that the small backswitched domains are of principal importance for wall propagation by the mechanism considered above in the section 5.4.

7 Formation and evolution of charged domain walls in congruent lithium niobate

It is well known that the charged domain wall has a very high surface energy due to the charge density of $2P_s$ on it. Therefore it is forbidden by the theory [30], but nevertheless any process of polarization reversal is realized through the formation and forward growth of spike-like nuclei with the charged domain wall. Moreover in some cases the as-grown domain structures contain a lot of stable charged domain wall, which can exist "forever" [31,32].

It was pointed by Myers thesis [33] that domains did not grow through the sample and the unswitched layer remained at Z^- surface for switching in CLN with metal electrodes. To our knowledge it is the only result of obtaining the stable charged domain wall in LN.

7.1 Formation of the charged domain wall

In this work the charged domain wall was obtained in standard optical-grade single-domain 0.2-mm-thick CLN wafers cut perpendicular to the polar axis. The transparent In_2O_3:Sn circular electrodes were deposited on Z^+ and Z^- surfaces. A high constant voltage pulse was applied to the substrate at room temperature. The evolution of the domain structure was visualized in crossed polarizers and the movie was recorded using the TV camera (Fig. 46).

Domains nucleated at the Z^+ surface, grow in the forward direction, but don't reach the Z^- surface, thus forming the stable charged domain wall (Fig. 47), which propagates in sideways direction. The strong fields produced by charged domain wall generate the variation of refraction index due to electrooptic effect, which allows to visualize the static and dynamic domain patterns (Fig. 48).

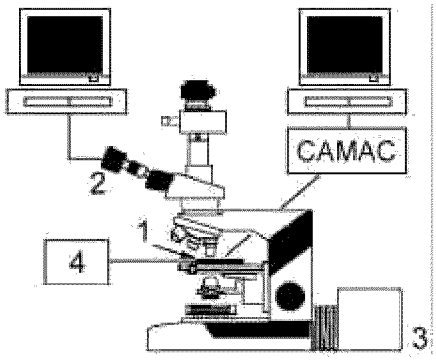

Figure 46 Experimental setup. 1 – sample, 2 – TV camera, 3 – lamp, 4 – high voltage supply.

The threshold field for charged domain wall formation by switching from the single-domain state is about 21 kV/mm and is about 17 kV/mm for the propagation of the existing charged domain wall. The relief of the charged domain wall essentially depends on the value of the applied field.

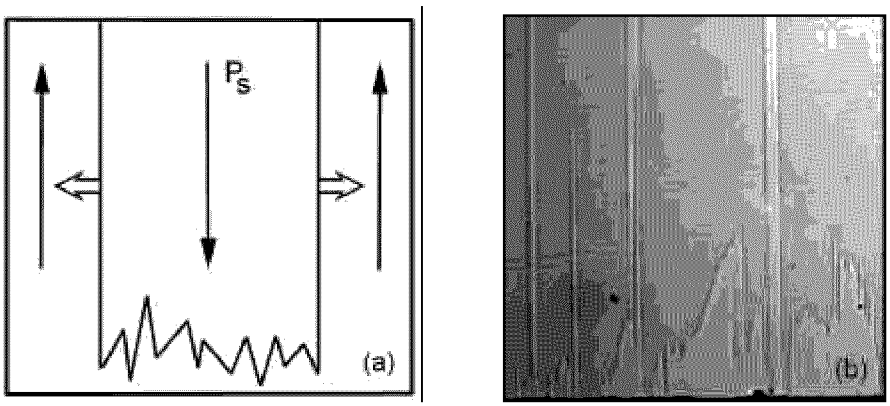

Figure 47 (a) – scheme of the charged domain wall (arrows show the directions of the domain broadening). (b) –charged domain wall on the **y**-surface of the sample (revealed by etching and visualized by optical microscopy).

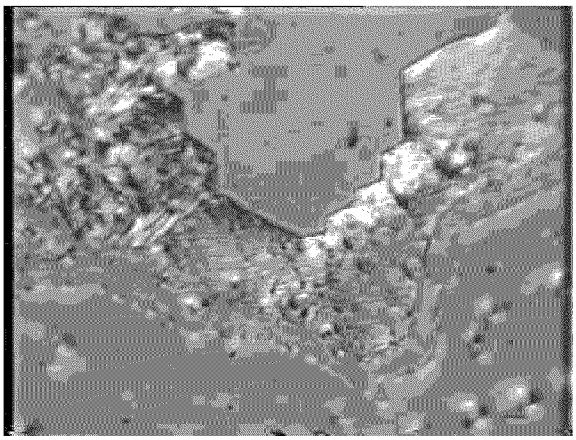

Figure 48 Charged domain wall pattern visualized in crossed-polarizers.

7.2 Sideways motion of neutral domain wall

The sequent positions of the neutral domain wall during its propagation (Fig. 49) were obtained from the sequence of frames taken from the movie. The neutral walls are oriented along the crystallographic directions of the crystal (Fig. 49).

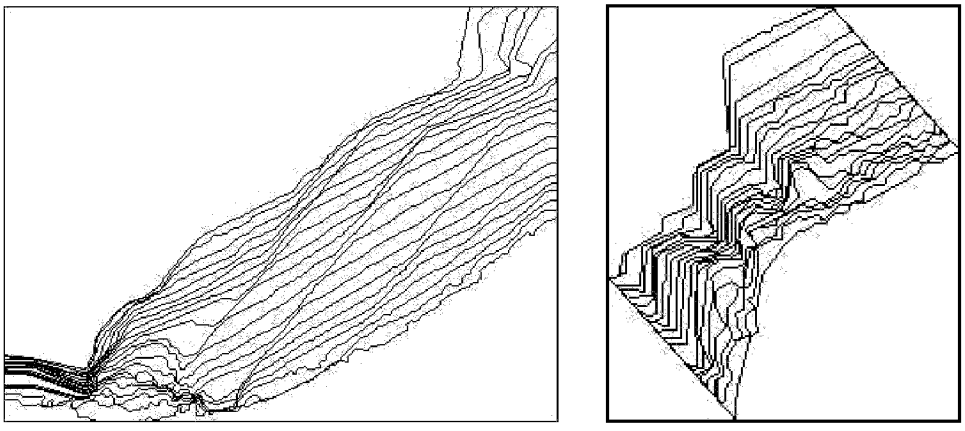

Figure 49 Sequent positions of the neutral domain wall during its motion in constant external field.

Velocity of the sideways wall motion appears to be spatially uniform with rare pinning of the wall at the local defects (Fig. 49a). The averaged values of the sideways wall motion velocity for the parts of the neutral wall determined from Figure 46 vary in the range of 40÷80 μm/s.

7.3 Field induced evolution of the charged domain wall

The field of the opposite direction was applied to the sample in order to switch the existing charged domain wall to initial state. The relief of the charged domain wall changes slightly at 10 kV/mm. The stages of the evolution of charged domain wall relief at 12.5 kV/mm presented on Figure 50. It must be pointed that the neutral domain wall does not move in backward direction in fields up to 22.5 kV/mm.

The image analysis of the sequent frames corresponded to the change of charged domain wall relief shows that the time dependence of transformed area S(t) follows the K-A formula for α(2D) process (Fig. 51):

$$S(t) = S\{1 - \exp[-(t/t_o)^2 (1 + t/t_m)]\} \qquad (10)$$

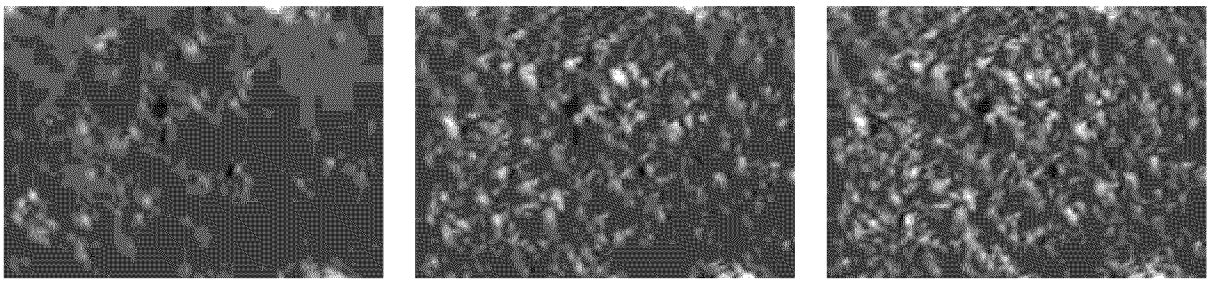

Figure 50 Evolution of the charged domain wall relief in CLN during switching in backward direction. The sequent frames for application of 12.5 kV/mm. Time interval 1 s. Domain patterns were visualized in crossed polarizers.

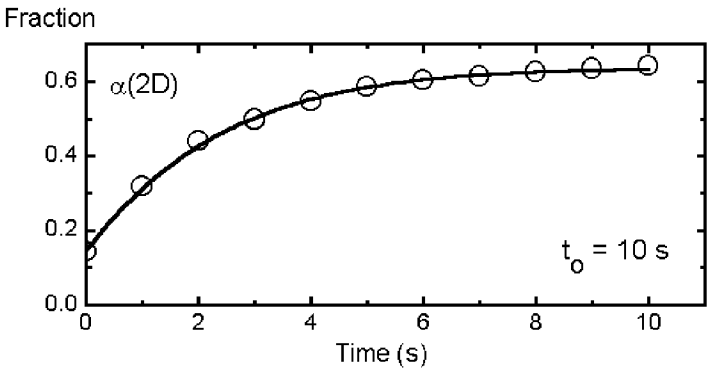

Figure 51 Time dependence of the charged domain wall transformed area in CLN in 12.5 kV/mm. Experimental points were fitted by Equation (10).

8 Periodical domain patterning in congruent lithium niobate and lithium tantalate

8.1 Domain shape during patterning in lithium niobate

The patterning under the periodic electrodes provides the anisotropic conditions for domain growth. Therefore the typical domain patterns contain the domains, which are not the regular hexagons, but all their walls are oriented strictly along the **Y** directions (Fig. 52).

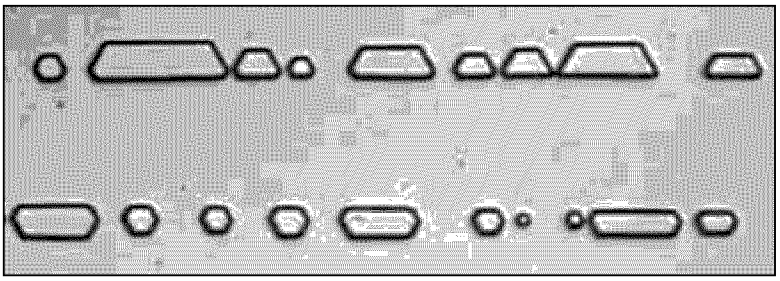

Figure 52 Typical domain shapes at $\mathbf{Z}^-$ surface during patterning in LN. Domain patterns revealed by etching were visualized by optical microscopy.

Comparatively rare the domains which appears as a result of switching in stronger fields demonstrate the triangular shape with domain walls oriented along **X** directions only (Fig. 53). This situation is similar to the effect of the influence of the field on the domain shape, which have been discovered by us in $Pb_5Ge_3O_{11}$ [34-36].

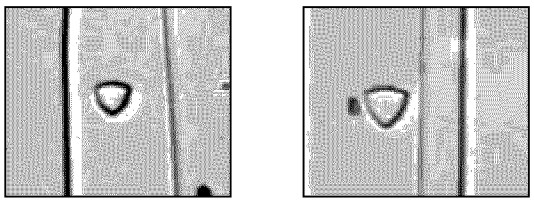

Figure 53 Triangular shaped domains at $\mathbf{Z}^-$ surface during patterning in CLN. Domain patterns revealed by etching were visualized by optical microscopy.

It must be pointed that even more complicated shapes with mixture of **X** and **Y** walls occur. For example, during patterning with periodical strip electrodes a “ship domains" with the mixture of hexagonal and triangular walls are frequently observed at $\mathbf{Z}^-$ surface (Fig. 54). Such behavior can be attributed to the strong field inhomogenety near the edges of the narrow strip electrode.

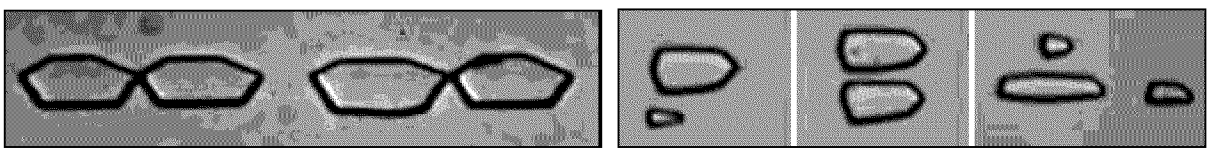

Figure 54 Mixed domain shapes at $\mathbf{Z}^-$ surface in CLN. Domain patterns revealed by etching were visualized by optical microscopy.

The irregular-shape residual domains were observed for domain wall coalescence at $\mathbf{Z}^-$ (Fig. 55). One can see that the domain wall orientations at these patterns do not exactly follow the crystallographic directions and can be attributed to the scenario of the domain evolution during switching.

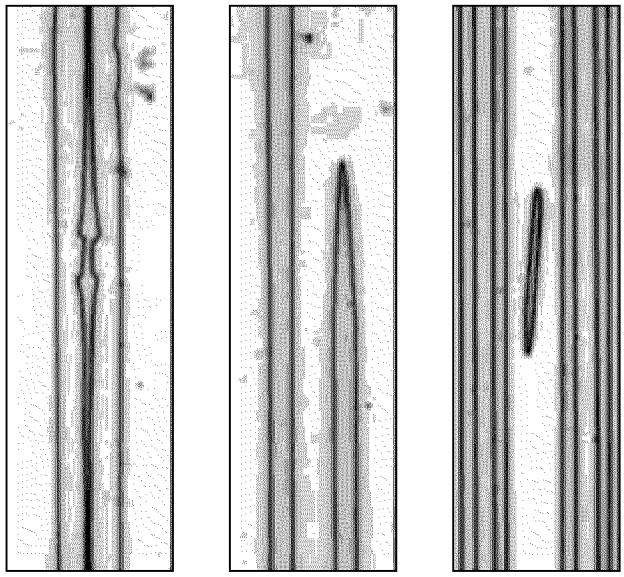

Figure 55 Deviations of the walls orientations from the crystallographic directions during coalescence in CLN ($\mathbf{Z}^-$ view). Patterns revealed by etching and visualized by optical microscopy.

Another example of unusual domain shapes - so called “star domains" is demonstrated at Figure 56. The wall orientation in this case strictly follows **Y** directions.

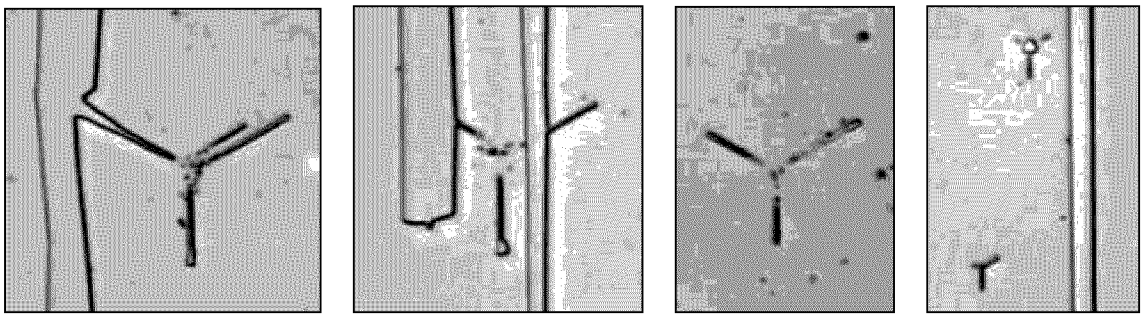

Figure 56 “Star” domains at $\mathbf{z}^-$ surface in CLN. Domain patterns revealed by etching and visualized by optical microscopy.

Even in uniform electric field the formed domain structures follow the crystal symmetry. The independent domains can “build” hexagons strictly oriented in the **Y** directions (Fig. 57).

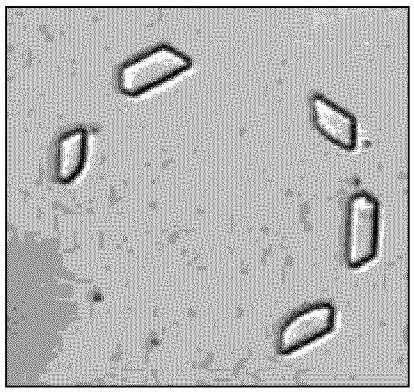

Figure 57 Structure of the individual domains in CLN which follow the crystal symmetry at $\mathbf{Z}^-$ surface. Domain patterns revealed by etching and visualized by optical microscopy.

8.2 Domain shape during patterning in lithium tantalate

The problem of formation of plane domain walls in CLT is more complicated than in LN due to triangular shape of individual domains. We carried out the observation of a great number of periodical short-pitch domain patterns in CLT. The typical results of domain wall formation on $\mathbf{Z}^-$ surface for 2.6 μm period is presented in Figure 58. Usually the individual domains do not merge (Fig. 58a). In the case of merging formed strip domains have only one plane wall (Fig. 58b). The rare strip domains with both plane walls never obtained for short-pitch patterning without local loosing the periodicity (Fig. 58b).

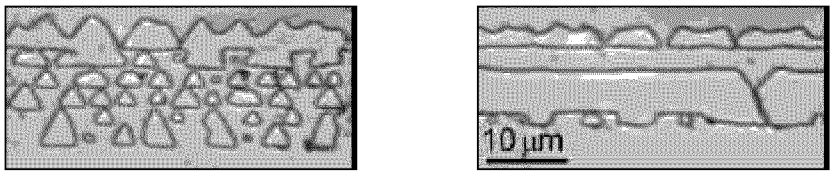

(a) (b)

Figure 58 Domain patterns in CLT. $\mathbf{Z}^-$ view. Domain patterns revealed by etching and visualized by optical microscope.

8.3 Spreading of the domain walls out of the electrodes in lithium niobate

8.3.1 Finger assisted domain wall motion

The scenario of the abnormal domain wall evolution during spreading in CLN was investigated using the tilted cross-sections (Fig. 59), which provides the time dependence of the wall structure. One can observe: 1) arising of periodic irregularities (Fig. 59a), 2) growth of oriented “fingers” (Fig. 59b,c), 3) merging of neighboring fingers (Fig. 59d,e,f). This process results in the anomaly large shift of the domain walls out of the electroded area.

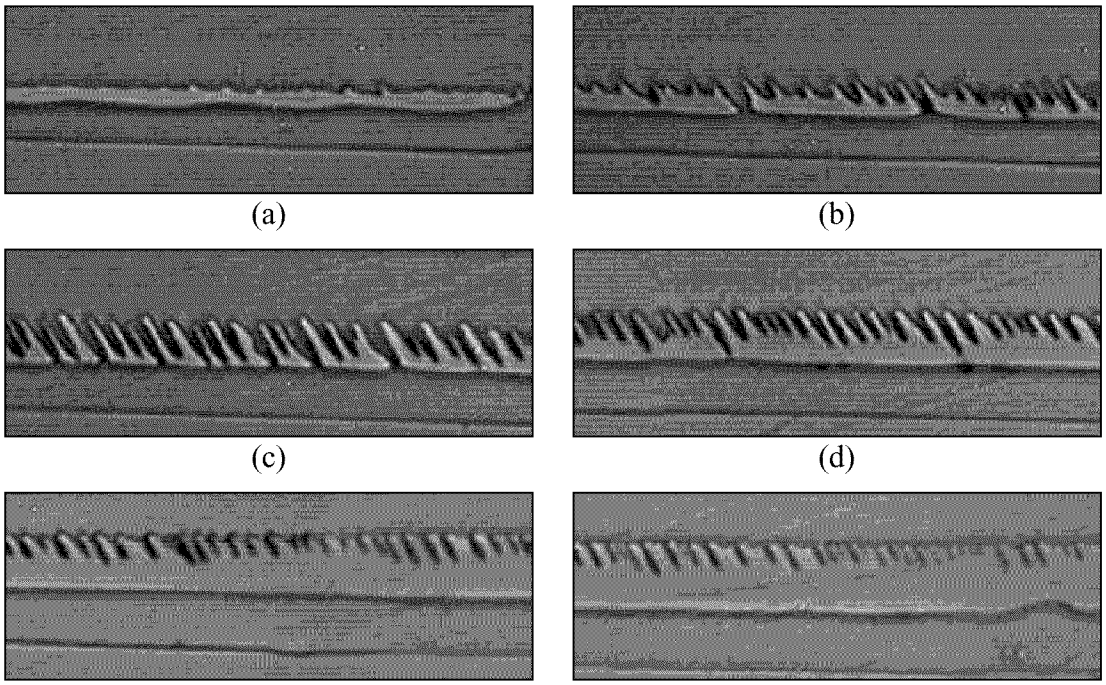

Figure 59 Stages of the domain wall evolution during finger-assisted spreading out of electrodes in CLN. Domain patterns revealed by etching were visualized by optical microscopy.

8.3.2 Switching current during patterning in lithium niobate with current limitation

During periodical domain patterning of large poling area the switching current reaches the current limitation of our power supply (about 20 mA). The observed difference between the programmed voltage waveform and the voltage measured at the sample is due to this limitation (Fig. 60). In this case we divide the voltage and current data into three stages. At the first stage ($\mathbf{t_{st} < t < t_1}$) the field at the sample and the current are constant. At the second stage ($\mathbf{t_1 < t < t_2}$) the field increases linearly and at the third ($\mathbf{t > t_2}$) the field becomes constant again and the current decreases (Fig. 60). The special mathematical treatment has been used for analysis of such current data.

As the electrode period Λ is very small in comparison with the sample thickness **d** the depolarization field is assumed to be spatially uniform and approximated by field in capacitor with effective charge equal to the sum of non-compensated charges at the nonelectroded area.

$$E_{dr}(\Delta x) = 2P_s/\varepsilon_o\varepsilon_i \cdot L_i/d \cdot 2\Delta x/\Lambda \qquad (11)$$

where ε_i – dielectric permittivity of the insulating layer.

Time dependence of the domain wall shift from the electrode edge $\mathbf{\Delta x}$ can be obtained from the switching charge data **Q(t)** in the following way

$$\Delta x(t) = 0.5[Q(t)\ (2P_s\ l)^{-1} - w_e] \qquad (12)$$

where **l** – total length of all domain walls, $\mathbf{w_e}$ – electrode width.

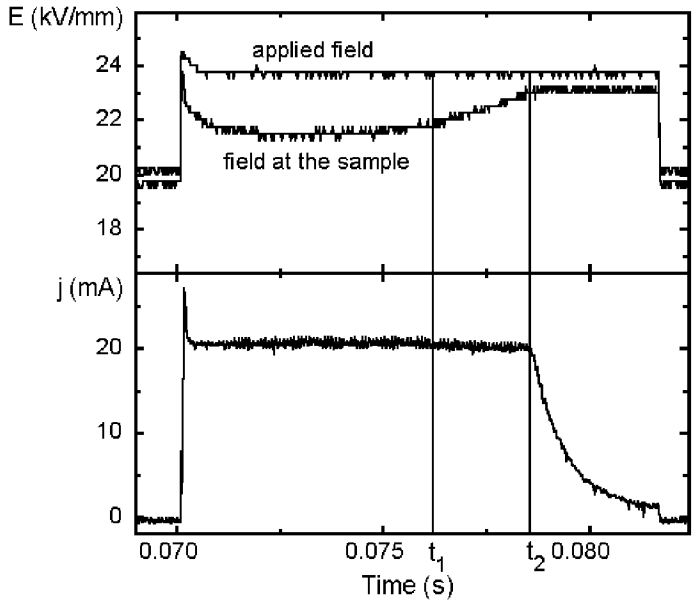

Figure 60 Field waveform and switching current for switching with current limitation in LN.

The value of the local field $\mathbf{E_z(\Delta x)}$ at the wall moving out of the electrode plays the role of the external field for switching in the middle of electrode. Thus such measurement appears to be a convenient method to determine in the single experiment the field dependence of the sideways wall motion velocity $\mathbf{v_s(E)}$.

After the complete switching under the electrodes $\mathbf{Q = 2P_s\ S}$ (**S** – total area of the electrodes) the switching current is proportional to $\mathbf{v_s}$ and **l**. Assuming the total length of the walls to be constant $\mathbf{v_s}$ is described by simple expression:

$$v_s(t) = j(t)\ (2P_s\ l)^{-1} \qquad (13)$$

The constant current means the constant velocity and hence the constant value of the local field. Therefore at the second stage ($\mathbf{t_1 < t < t_2}$) the variation of the field at the sample should be equal to the depolarization field. But it was found out that the ratio of the variation of the field at the sample and depolarization field obtained from Equation (11) is equal to 0.06. This fact can be explained in terms of partial screening of depolarization field by charge injection through the insulating layer just after the polarization reversal. This effect is quite realistic, as the field in the layer is super strong (about 30000 kV/mm). Charge injection leads to the effective "decrease" (compensation) of the bound charges and hence decreases the depolarization field. Thus about 94% of depolarization field is compensated by the charge injection through the insulating layer.

Using all aforementioned considerations the field dependence of the sideways wall motion velocity was obtained (Fig. 61) and main parameters of the domain kinetics were extracted from the approximation – the start field $\mathbf{E_{st}}$ = 21.2 kV/mm and the mobility of the domain wall μ = 1.2 10^{-5} cm^2/Vs.

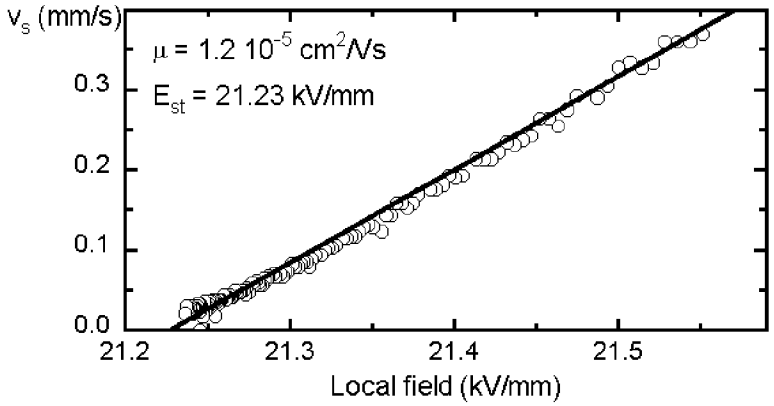

Figure 61 Field dependence of the sideways domain wall motion velocity out of the electrodes in LN. Experimental points were fitted by linear field dependence.

The limit value of the sideways wall motion velocity $\mathbf{v_{s\ lim}}$ = 0.37 mm/s is about the wall velocity at the electrode edges for switching without current limit $\mathbf{v_s}$ = 0.51 mm/s.

8.3.3 Calculation of the domain wall spreading out of the electroded area

Spreading of the formed domain walls out of electrodes for thick sample (the electrode period Λ << **d**) can be considered as a domain wall motion in uniform electric field. It is clear that the spatial inhomogeneity of external field $\mathbf{E_{ex}}$, which is so important for nucleation, exists only in the surface layer with the thickness of about several Λ.

The wall velocity is determined by the polar component of the local electric field $\mathbf{E_z}$ [10]. The ratio of compensation of depolarization field by external screening in the area between metal electrodes by charge redistribution at the liquid electrodes is smaller as compare with the compensation under the metal electrodes (Fig. 62). This effect and comparatively slow bulk screening in LN at room temperature lead to decrease of $\mathbf{E_z}$ during shifting due to increasing of uncompensated part of depolarization field. The domain wall stops when

$$E_z(\Delta x) - E_{st} \sim 0 \qquad (14)$$

where $\Delta\mathbf{x}$ – shift of the domain wall out of electrode.

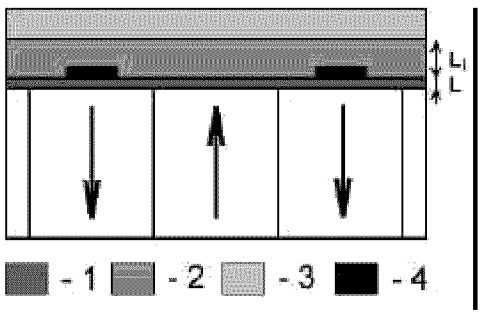

Figure 62 Scheme of the surface region of the substrate with electrodes (1 – dielectric gap, 2 – insulating layer, 3 – liquid electrolyte, 4 – metal electrodes).

Assuming that conductivity of insulating layer and bulk screening can be ignored and that the thickness of insulating layer $\mathbf{L_i} >> \mathbf{L}$ the dependence of average bulk value of $\mathbf{E_z}$ on $\Delta\mathbf{x}$ for used experimental setup (Fig. 62) can be estimated. The decrease of $\mathbf{E_z}$ during motion occurs due to the increasing of depolarization field $\mathbf{E_{dr}(\Delta x)}$ and the field produced by the "frozen" bulk screening charges (memory effect). If the spatial distribution of the charge is approximated by two stripes of the width $\Delta\mathbf{x}$ with effective surface charge density σ, then the shift dependence of the field at the domain wall is given by Equation (11), which allows to determine the field dependence of the domain shift out of electrodes $\mathbf{\Delta x(E_{ex} - E_{th})}$.

Taking into account the field dependence of the domain wall velocity for periodical switching the simulation of the switching process was carried out. The model parameters were taken as follows: $\mathbf{P_s}$ = 78 μC/cm^2, $\mathbf{d}$ = 0.5 mm, $\mathbf{L_i}$ = 0.5 μm, ε_i = 3.1, Λ = 4 μm, $\mathbf{w_e}$ = 0.8 μm, S = 300 mm^2, $\mathbf{k}$ = 0.06, μ = 1.2 10^{-5} cm^2/Vs, $\mathbf{E_{st}}$ = 21.2 kV/mm, $\mathbf{E_{ex}}$ = 22 kV/mm. The dependencies of the sideways domain wall velocity on time (Fig. 63) and shift (Fig. 64) were obtained.

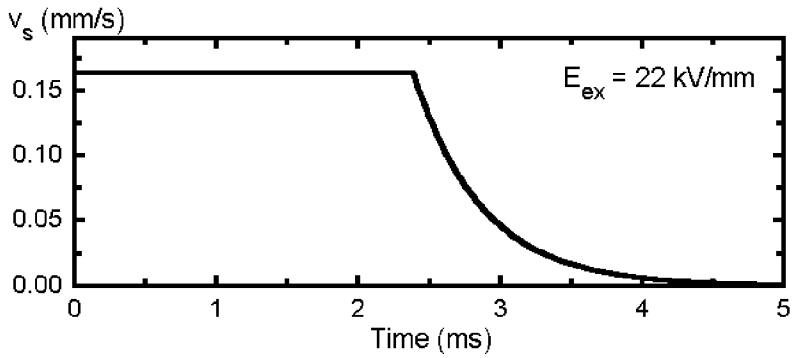

Figure 63 The simulated time dependence of the sideways domain wall velocity for E_{ex} = 22 kV/mm.

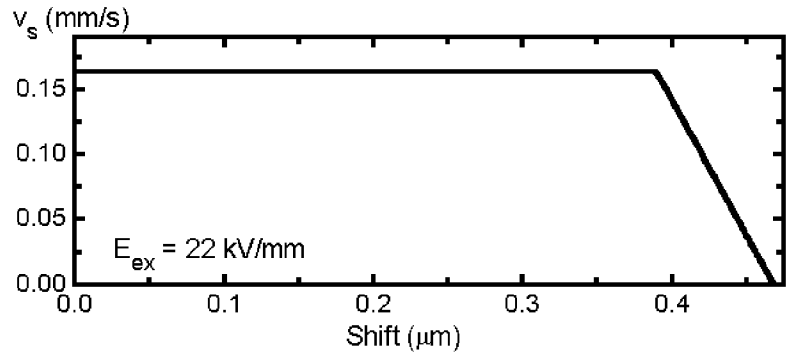

Figure 64 The simulated shift dependence of the sideways domain wall velocity for E_{ex} = 22 kV/mm.

The similarity of the simulated wall velocity time dependence (Fig. 63) and the experimental data (Fig. 60) shows that the proposed model can be successfully used to describe the domain wall motion out of electrodes during periodical patterning.

8.4 Domain walls interaction during coalescence

Domain spreading out of electrodes is essentially unpleasant for short pitch patterning as it can result in complete merging of the neighboring domain walls. It is clear that depolarization field produced by the neighboring domain influences the domain walls motion. When the walls come together the depolarization field doubles and the velocity of the domain wall decreases. Examples of the domain-domain interaction can be seen at Figure 65.

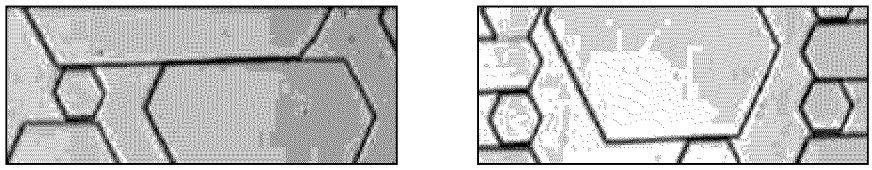

Figure 65 Domain-domain interaction at $\mathbf{Z}^-$ surface in CLN. Domain patterns revealed by etching and visualized by optical microscopy.

The conditions for coalescence of the domain walls at $\mathbf{Z}^+$ and $\mathbf{Z}^-$ surfaces differ essentially due to different electrode configurations. Domain walls at $\mathbf{Z}^-$ surface move in uniform field with fast enough screening. Therefore even just before coalescence distance between them is uniform and residual narrow domain looks like a thin line which vanishes uniformly (Fig. 66a,b).

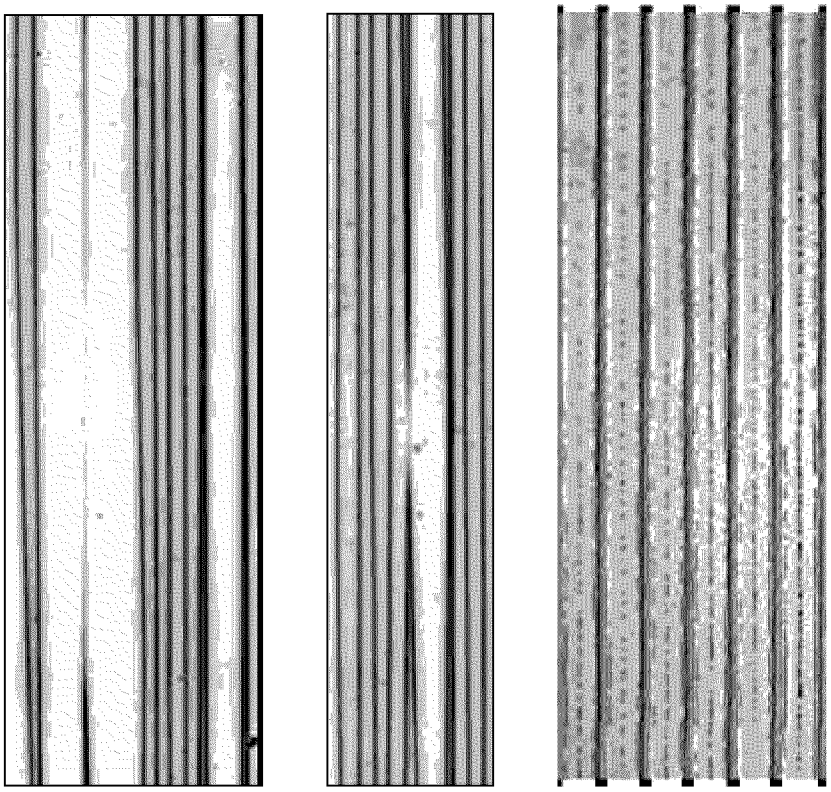

Figure 66 Domain walls coalescence out of electrodes in CLN (a), (b) at $\mathbf{Z}^-$ surface; (c) at $\mathbf{Z}^+$ surface. Black rectangles show the positions of electrodes. Domain patterns revealed by etching and visualized by optical microscopy.

The wall's coalescence scenario at $\mathbf{Z}^+$ surface is drastically different due to very slow screening between the electrodes. Just before coalescence the narrow residual domain starts to "tear" in dashes and dots (Fig. 66c).

8.5 Frequency multiplication of periodical domain patterns

We have studied in details the special process of domain evolution during backswitching, which leads to spatial frequency multiplication of domain pattern as compare with the electrode one. The mechanism of frequency multiplication is based on the nucleation along the electrode edges during backswitching (Fig. 67a), while the role of the wall motion in this case is negligible.

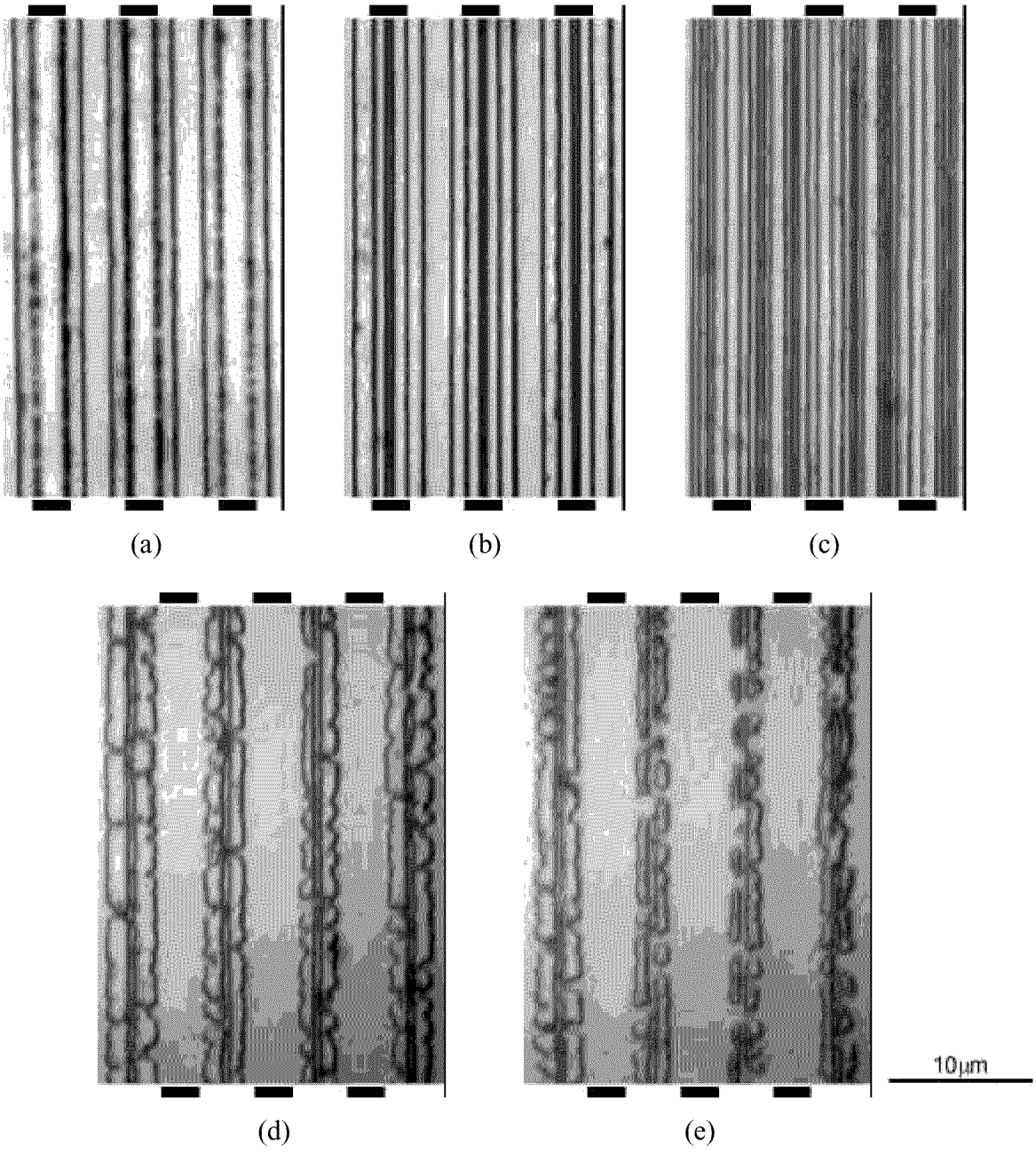

Figure 67 Stages of domain evolution during domain frequency multiplication process in CLN. $\mathbf{Z}^+$ view. Domain patterns revealed by etching and visualized by optical microscope.

For "frequency tripling" (Fig. 68) the subsequent growth and merging of nucleated domains lead to formation of a couple of strictly oriented sub-micron-width domain stripes under each electrode (Fig. 67b, 69a). The width of the stripes increases during backswitching and can be controlled by duration of backswitching stage. The typical depth of the backswitched domain stripes is about 20 - 50 μm (Fig. 69b). It is clear that this structure can be produced only using wide enough electrodes.

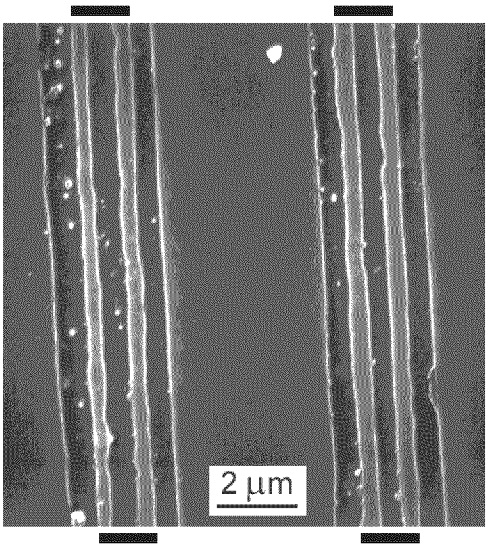

Figure 68 SEM image of domain “frequency tripling” in CLN. $\mathbf{Z}^+$ view.

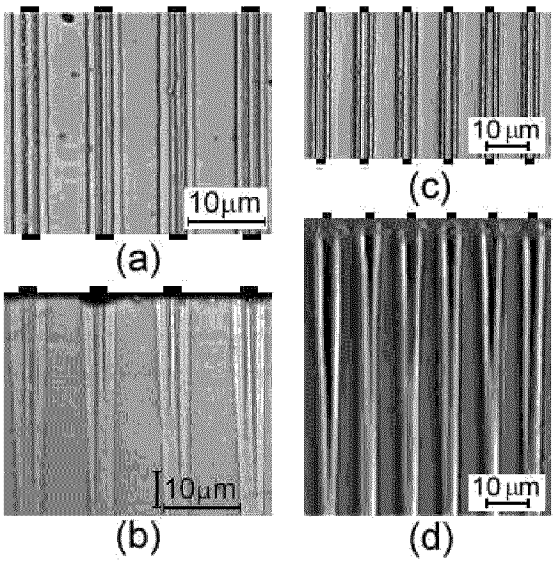

Figure 69 Domain frequency multiplication in CLN. Domain “frequency tripling ”: (a) - $\mathbf{Z}^+$ view and (b) - **Y** view. Domain “frequency doubling ”: (c) - $\mathbf{Z}^+$ view and (d) - **Y** view**.** Patterns revealed by etching and visualized by optical microscope.

For narrow electrodes and long enough backswitching time these stripes merge and only the "frequency doubling" can be obtained (Fig. 69c). The depth of backswitched domain stripes for doubling is typically about 50 - 100 μm (Fig. 69d). The final stage of backswitching presents

the merging of wide backswitched domains with residual ones (Fig. 67d,e). Finally it leads formation of completely single domain state just as before switching.

9 Nanodomain engineering in lithium niobate

We discovered that the evolution of domains during backswitching in CLN is a highly organized process. This spontaneous decay of laminar domain structure proceeds through arising and growth of oriented nanoscale domain arrays contrary to expected trivial backward motion of the existing domain walls accompanied by random nucleation of new domains. Domain evolution during backswitching strongly depends on the value of domain wall shift out of electroded area during "high field" stage. Moreover such parameters of voltage waveform as the duration of "high field" stage Δt_{sp} and the value of the jump from "high" to "low" field (field-diminishing amplitude) ΔE allow to control the backswitching kinetics. Three main scenarios of highly organized domain evolution can be revealed (Fig. 70-72).

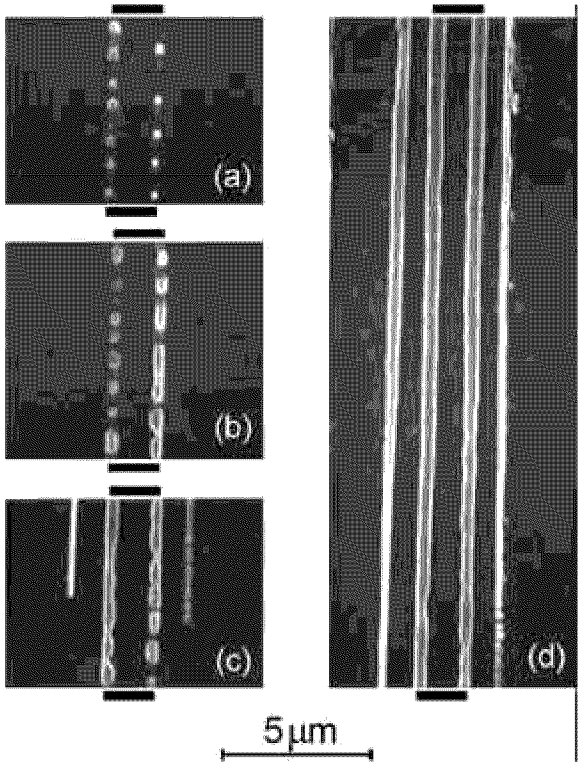

Figure 70 SEM domain images demonstrating the stages of the formation of periodic strip domains along the electrode edges. Black rectangles show the positions of the electrodes

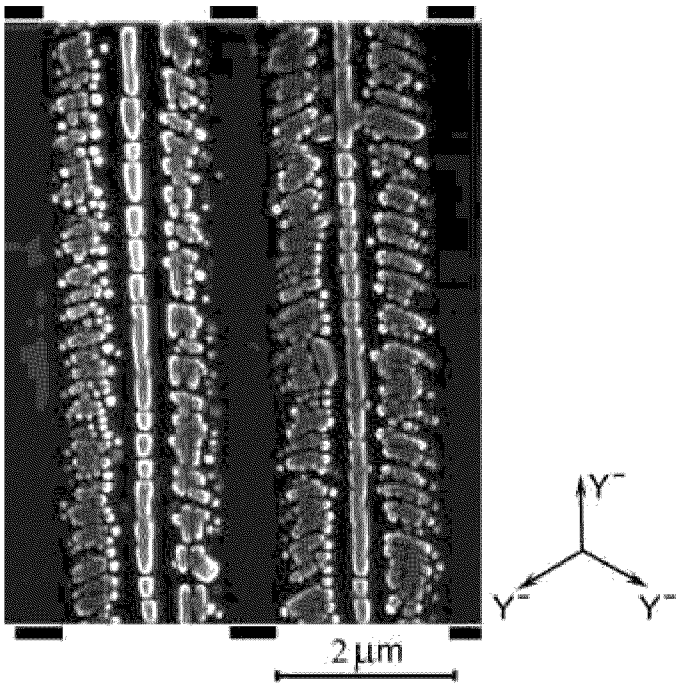

Figure 71 SEM images of nanodomain arrays oriented along $\mathbf{Y}^{-}$ directions at 60 degrees to the electrode edges. $\mathbf{Z}^{+}$ view. Electrodes cover the area between black rectangles. Domain patterns revealed by etching.

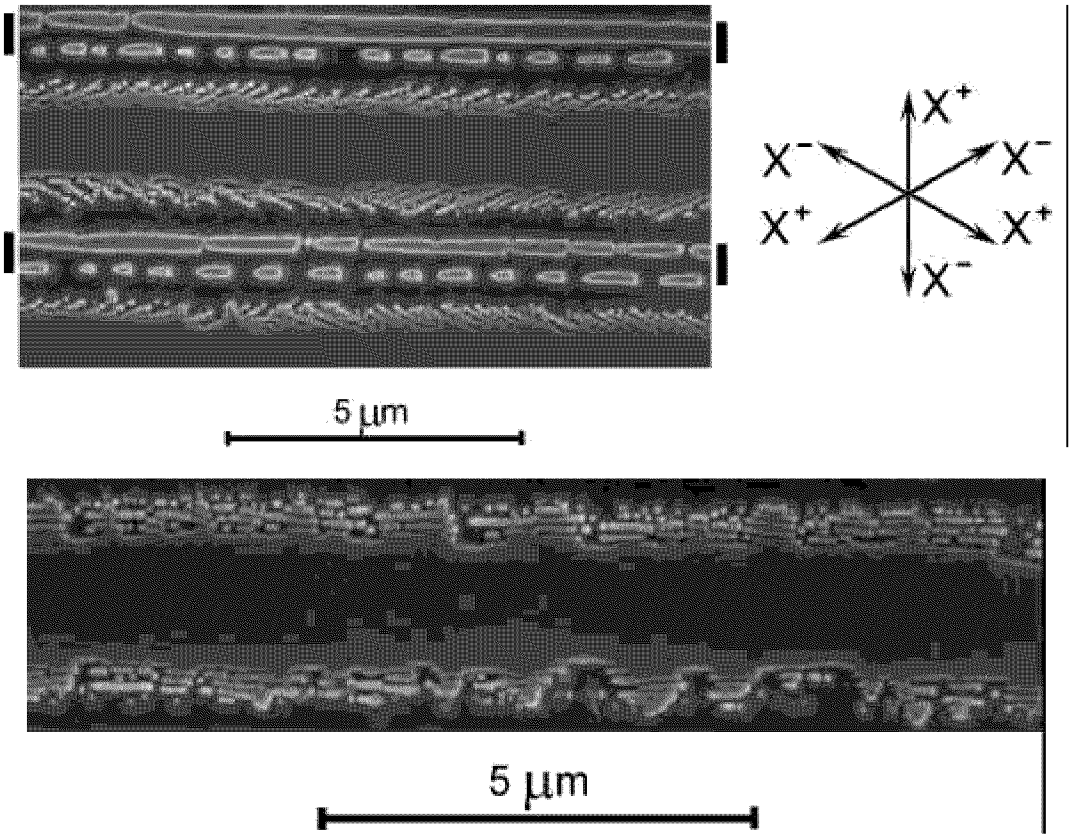

Figure 72 SEM images of nanodomain arrays oriented along **X** directions at 30 and 90 degrees to the electrode edges. $\mathbf{Z}^{+}$ view. Electrodes cover the area between black rectangles. Domain patterns revealed by etching.

9.1 Formation of periodic strip nanodomain structures

In the samples with large period of electrode structure (more than 7 μm) for long switching pulse Δt_{sp} ~ 15 ms the wall shift out of electroded area exceeds 3 μm. In this case for high field-diminishing amplitude ΔE ~ 20 kV/mm the backswitching leads to the formation of the periodic strip domains oriented along the electrodes (Fig. 70). Formation of this structure starts with arising of a couple of 1D-nanodomain arrays strictly under the electrode edges (Fig. 70a). Image processing demonstrates the strong correlation of spatial distribution of arisen nanodomains (average distance between neighbors is about 200 nm). These arrays turn into a pair of strip domains through growth and merge of nanodomains (Fig. 70b). After their complete merging a new couple of 1D nanodomain arrays appears in nonelectroded area parallel to the first one at the distance about 1 μm (Fig. 70c). On this way it is possible to demonstrate the "frequency pentaplication" effect (Fig. 67c). The distance between secondary and initial stripes is about the thickness of the artificial insulating layer. Therefore we can change the period of the structure by controlling the thickness of insulating layer.

9.2 Formation of the quasi-periodical structure of oriented nanodomain arrays

Spontaneously arisen domain structure for short electrode periods (less than 4 μm) is drastically different. Domain patterns visualized by SEM and SFM demonstrate the highly organized quasi-periodical structure of domain arrays (Fig. 71-75). Each array is always oriented along determined crystallographic direction. Two variants of array orientation have been obtained under different switching conditions.

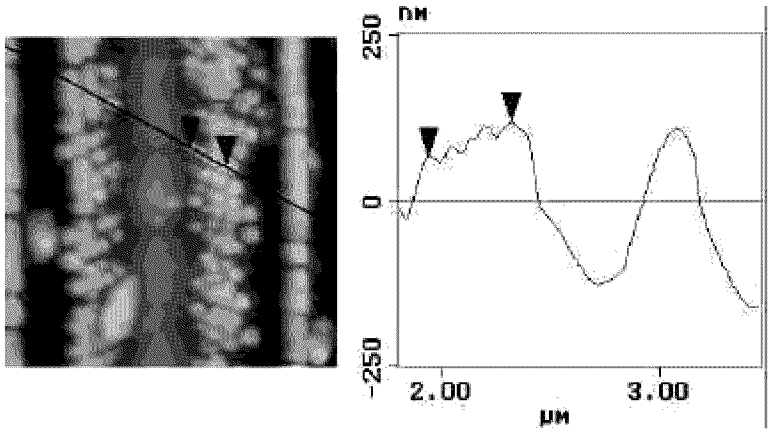

Figure 73 SFM image of nanodomain arrays oriented along $\mathbf{Y}^-$ directions at 60 degrees to the electrode edges with profile along **Y** direction. Domain patterns revealed by etching. $\mathbf{Z}^+$ view.

For short switching pulse duration Δt_{sp} ~ 5 ms and the low field-diminishing amplitude ΔE ~ 2 kV/mm the domain arrays are oriented strictly in one of three **Y** [•• $\bar{\bullet}$ •] directions (Fig. 71,73) at 60 degrees to the electrode edges. Each quasi-regular array is comprised of the

nanoscale domains with diameters 30-100 nm and average linear density exceeding $10^4 mm^{-1}$. In contrast to large electrode periods the nucleation along the electrode edges have been never observed (Fig. 70a).

For long switching pulse duration Δt_{sp} ~ 5 ms and the high field-diminishing amplitude (ΔE > 10 kV/mm) the domain arrays are oriented strictly in one of six **X** [• $\bar{•}$ $\bar{•}$ •] and [•• $\bar{•}$ •] directions (Fig. 72,74). The individual nanoscale domains are triangular shaped and their sizes are about 30-100 nm (Fig. 75). In addition the nucleation along electrode edges and consequent formation of strip domains is observed.

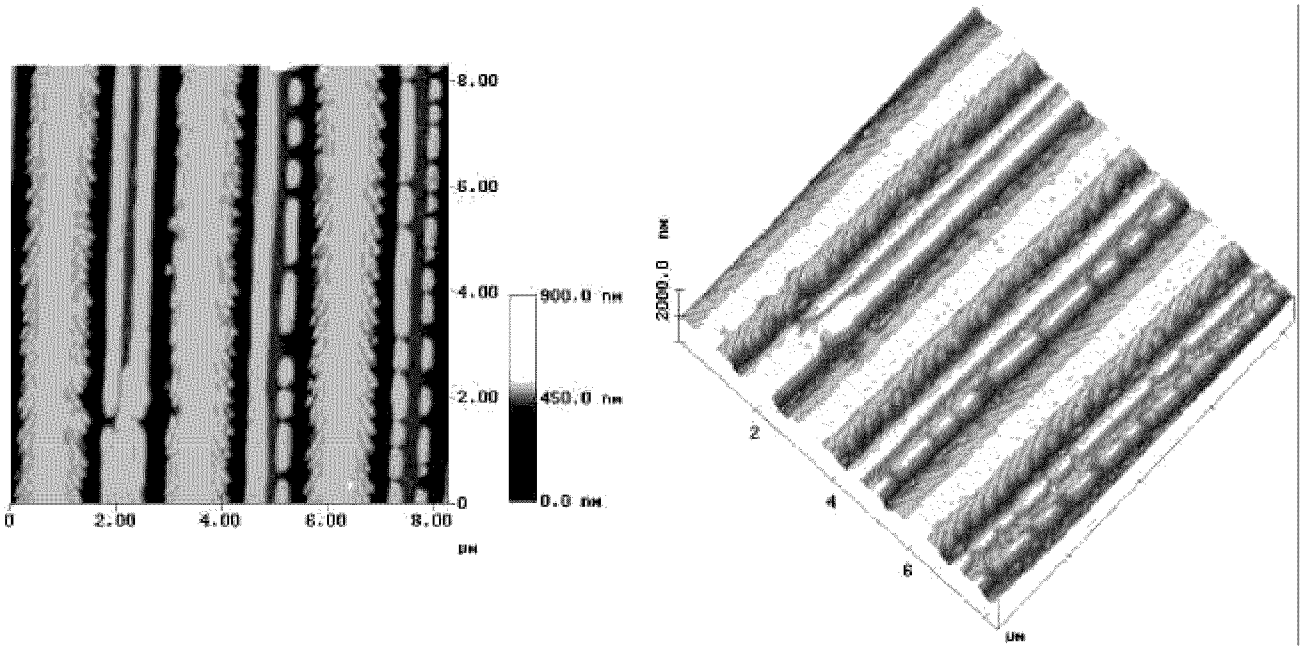

Figure 74 SFM images of nanodomain arrays oriented along **X** directions at 30 and 90 degrees to the electrode edges. $\mathbf{Z}^+$ view. Domain patterns revealed by etching.

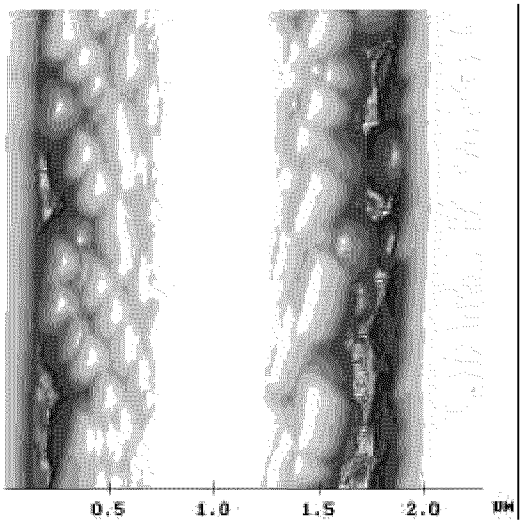

Figure 75 SFM image of nanodomain arrays oriented along **X** directions at 30 degrees to the electrode edges. $\mathbf{Z}^+$ view. Domain patterns revealed by etching.

9.3 Physical basis of nanodomain engineering

All observed results can be explained under the preposition that the switching process in the given place is driven by the polar component of the local electric field E_z. The value of local field E_z depends on the instantaneous domain pattern and screening degree. E_z is defined by the sum of polar components of external field E_{ex}, depolarization field E_{dep} and various screening fields E_{scri}

$$E_z(r,t) = E_{ex}(r) - E_{dep}(r,t) - \Sigma E_{scri}(r,t) \qquad (15)$$

In the case of strip electrodes E_{ex} is essentially inhomogeneous with strong increase in the surface layer along the electrode edges due to the fringe effect. The depolarization field E_{dep} is produced by bound charges and always hampers the domain growth. It tends to reconstruct the initial domain pattern when the E_{ex} is switched off. It is clear that for multi-domain state E_{dep} is essentially inhomogeneous. Both fields are compensated by screening processes.

Just after mainly the current in the external screens switching the arising E_{dep} circuit (external screening). The degree of fast screening and therefore the value of residual depolarization field depend on the ratio between thickness of sample and dielectric layer (Fig. 76a) [22]

$$E_{rdep} = L/d\ Ps/\varepsilon\varepsilon_o \qquad (16)$$

In used experimental geometry (Fig. 76a) the thickness of dielectric layer is spatially nonuniform. Under the electrodes the thickness is determined by the sub-micron intrinsic layer (dead layer) L_{in} and out of electrodes by deposited 1 μm-thick isolating layer L_{is}.

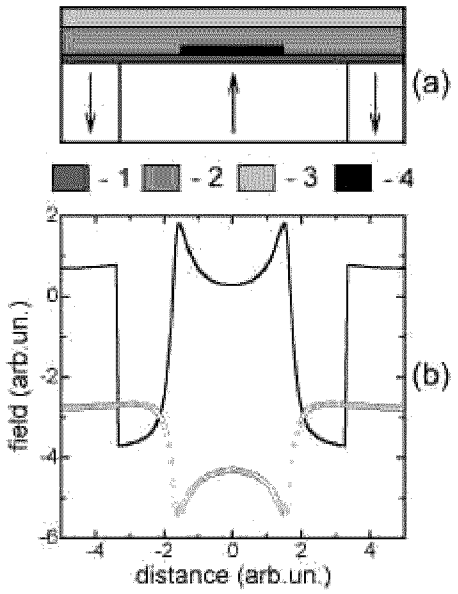

Figure 76 (a) Surface region of the substrate with strip electrode: 1 - dielectric gap, 2 - insulating layer, 3 - liquid electrolyte, 4 - metal electrode. (b) Calculation of the spatial distribution of backswitching field near $\mathbf{Z}^+$ surface: in two limiting cases (solid line - low ΔE and short switching pulse Δt_{sp}, points - high ΔE and long Δt_{sp}).

The bulk screening processes compensate the residual part of the local field E_{zr}

$$E_{zr}(r,t) = E_{ex}(r) - (E_{dep}(r,t) - E_{screx}(r,t)) \quad (17)$$

In wide switched domain (Fig. 76b) the E_{zr} under the electrodes is much less than out of electroded area since $L_{in} << L_{is}$.

The bulk screening process is slower and determined by redistribution of bulk charges, reorientation of the defect dipoles and injection from electrodes through the insulating layer during switching [12,13]. As a result the field spatial distribution after removing of external field depends on the duration of switching pulse and field decreasing amplitude (Fig. 2).

9.4 Correlated nucleation under the electrode edges

In order to explain why the nucleation starts under the electrode edges we calculate the spatial distribution of field polar component of $\mathbf{E_Z}$ in sample with periodical electrodes (Fig. 77). As it was anticipating this distribution demonstrates sharp singularities under the edges of finite electrodes. It must be pointed out that spatially nonuniform $\mathbf{E_Z}(x,y)$ exists only in the vicinity of the surface and its amplitude rapidly decreases with the depth (Fig. 77). Practically uniform field is obtained at the depth about the electrode period. Such estimations clarify the cause of observed spatially nonuniform nucleation in thin surface layer and show that subsequent growth of domains in the bulk goes on in uniform electric field.

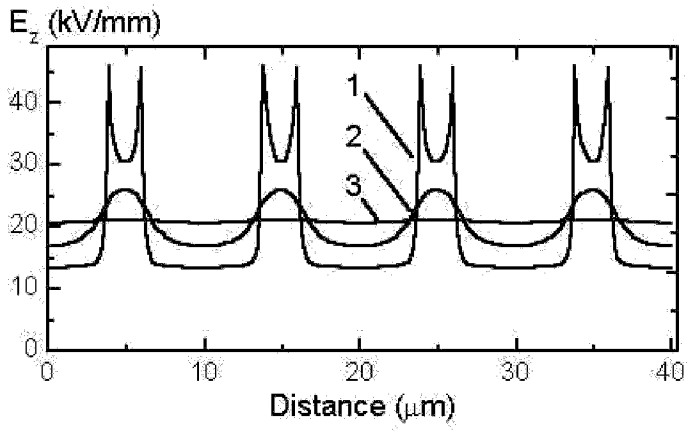

Figure 77 Calculated spatial distribution of the field polar component E_Z near $\mathbf{Z^+}$ surface in sample with periodical electrodes.

The switching current recorded while applying the switching pulse gives the additional information about the nucleation and forward growth processes (Fig. 78). Two important moments of domain evolution can be clear extracted. Up to the first one $\mathbf{t_1}$ the current demonstrates quadratic time dependence. This fact can be explained in assumption of correlated nucleation at constant nucleation rate (α process). Thus first part of current pulse corresponds to

independent growth of isolated domains under the edges of electrodes which start to merge at moment $\mathbf{t_1}$. At the second moment $\mathbf{t_2}$ the domains reach $\mathbf{Z^-}$. It is clear that

$$t_1 = \frac{\Delta y}{2V_s} \tag{18}$$

$$t_2 = \frac{d}{V_f} \tag{19}$$

where $\Delta\mathbf{y}$ - the average distance between the nuclei, $\mathbf{V_s}$ - velocity of sideways domain growth under the edges of electrodes, $\mathbf{V_f}$ - velocity of forward growth (tip propagation).

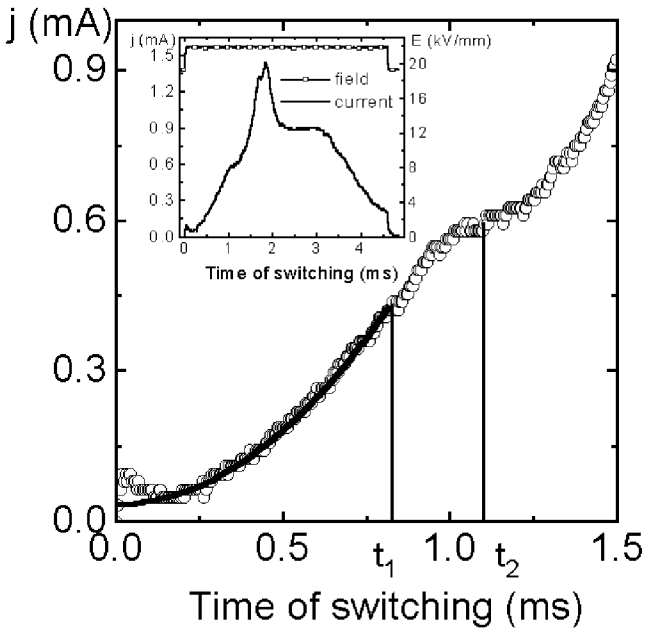

Figure 78 Switching current corresponding to growth and merging of isolated domains under the electrode edges in CLN. In the inset – whole current pulse and applied field.

The knowledge of these time intervals allows to determine the values of the most important velocities characterizing sideways domain wall motion and tip propagation. The results of the analysis of experimental data for about ten samples with wide variety of electrode width and period are summarized in Table 5.

Table 5. The velocities of wall motion and tip propagation in CLN.

Forward growth velocity	304 ± 29 mm/s
Sideways wall motion velocity at electrode edges	0.51 ± 0.04 mm/s

9.5 Mechanism of correlated nucleation

It is obvious that understanding of correlated nucleation mechanisms needs the knowledge of spatial distribution of the local field polar component. We suppose that the peculiarities of

external screening play a principal role in this effect. In order to verify this hypothesis the spatial distribution of local field produced by individual strip nonthrough domain located at the surface was calculated for the infinite plate completely covered by uniform electrodes (Fig. 79). The maximums of residual depolarization field $\mathbf{E_{dr}}$ are observed at the distance of about thickness of dielectric gap **L** from domain wall (Fig. 79, 80a).

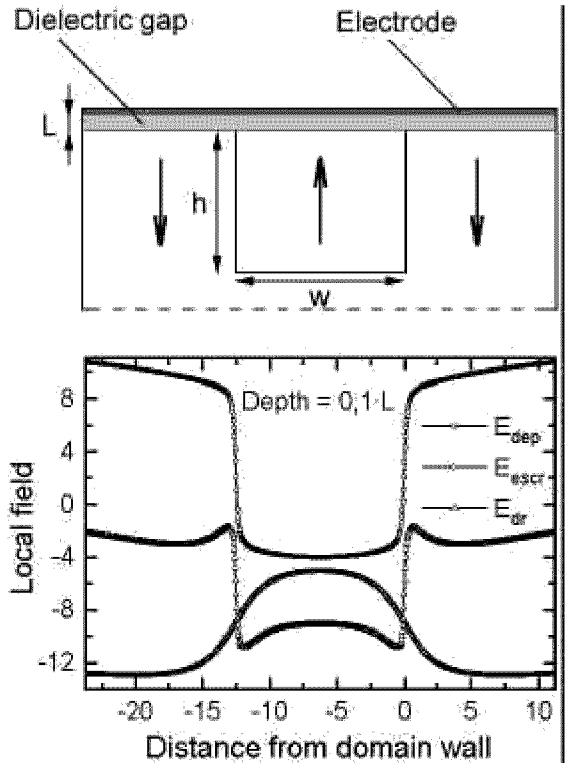

Figure 79 Scheme of the surface layers and the spatial distribution of depolarization and screening fields caused by strip domain. Distance from the domain wall and depth from the dielectric gap are given in units of dielectric gap thickness L. Domain sizes **h** = **w** =12.5·L.

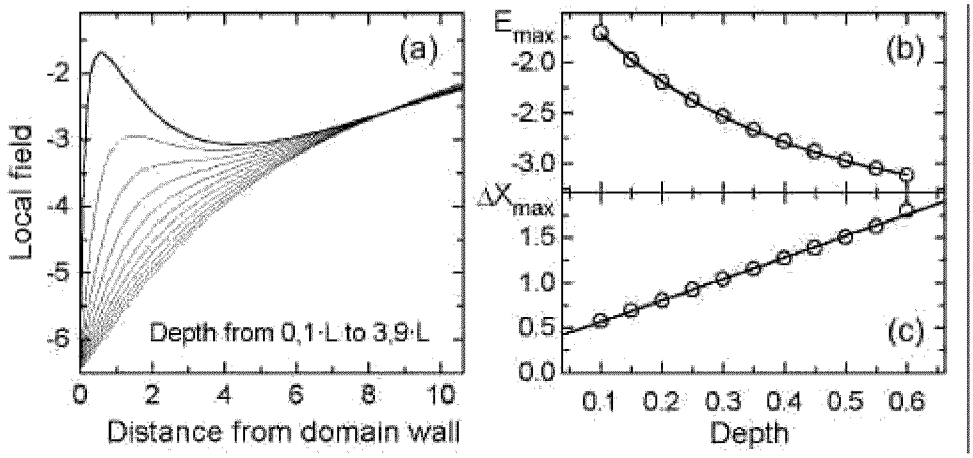

Figure 80 Change of spatial distribution of the local field produced by strip domain for different depth from the dielectric gap (a). Dependence on the depth of local field maximum (b) and the distance from the position of local field maximum to the wall (c)

It was found from this calculation that local field maximums exist only near the surface just under the dielectric gap and disappear at the depth of the order of **L** (Fig. 80a,b). The value of maximum decreases proportionally to the reciprocal value of the depth (Fig. 80b) and the distance from the domain wall to field maximum linearly increases with depth (Fig. 80c). These results allow to explain the effect of correlated nucleation. It is clear that the position of the nucleation site must correspond to the field maximum because the local field near the surface determines the nucleation probability. Many evidences of correlated nucleation were observed in CLN during switching in uniform field. One of the common manifestations of this effect is the arising of the nuclei at short distance from the plane domain wall (Fig. 81). It was shown also that the correlated nucleation plays important role during backswitching.

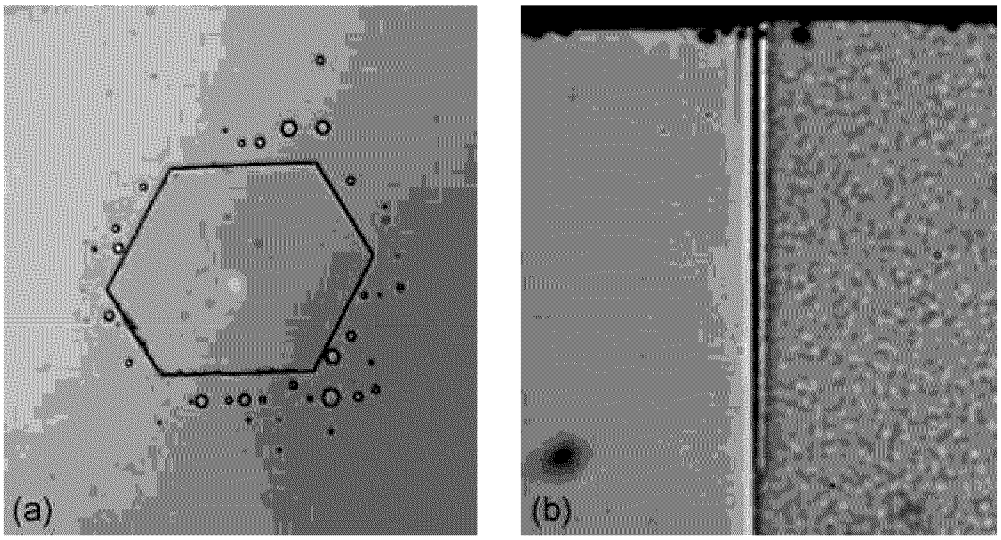

Figure 81 Formation of nuclei near the plane domain wall. (a) **Z** view, (b) **Y** view. Domain patterns revealed by etching and visualized by optical microscope.

10 Short-pitch domain patterns in lithium niobate and lithium tantalate

10.1 Application of the backswitched poling for 2.6 μm patterning in lithium niobate

We have applied the backswitching method for 2.6-μm periodical poling of the CLN 0.5-mm-thick substrates. It is seen that the domain patterns on $\mathbf{Z}^-$ are practically ideal (Fig. 82). Such domain structure was prepared in fragments of 3-inch-diameter substrate. It must be pointed out that to our knowledge all to date attempts to produce the periodic domain structures with such period in 0.5-mm-thick CLN by conventional poling method have not met with success.

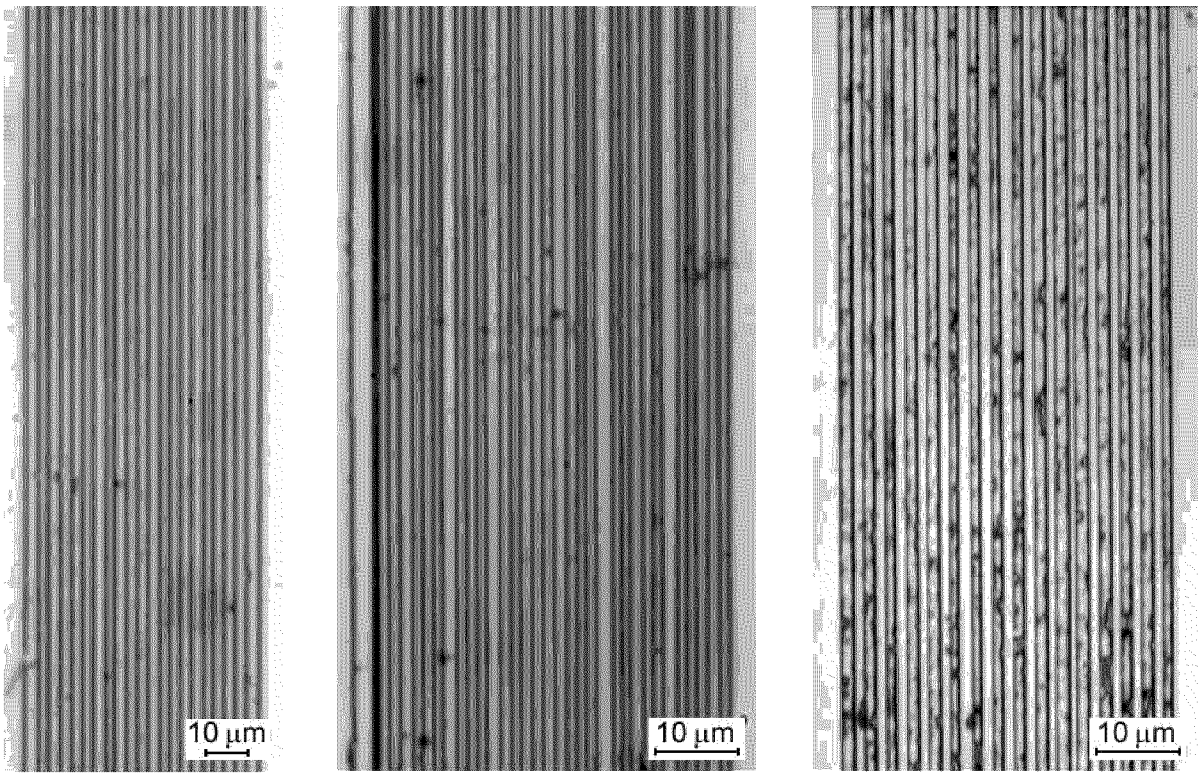

Figure 82 Domain patterns in CLN for 2.6 μm period for $\mathbf{Z}^-$ view revealed by etching were visualized by optical microscopy.

10.2 Quasi-phasematched generation in backswitched-poled lithium niobate

The continuous-wave single-pass second harmonic generation in 4-μm-period 0.5-mm-thick backswitched-poled CLN was obtained [37-39]. Using this material, 50-mm-length devices where characterized for continuous wave (CW) single-pass second harmonic generation of blue light [40,41]. Using the CW Ti:sapphire pump laser near confocally focused to a 44 μm waist radius in the center of the sample, 6.1%/W efficient first-order generation of 61 mW at $\lambda = 460$ nm was achieved, indicating an effective nonlinearity $d_{eff} \approx 9$pm/V, approximately one half of the nominal value. The obtained nearly ideal tuning curve for 460 nm second harmonic generation phase matching versus temperature, indicating that the sample phase matches nominally over the full 50 mm length [40,41].

Moreover laser-diode-pumped second harmonic generation was performed with an antireflection-coated InGaAs single-stripe diode master oscillator (SDL prototype) in a Littman external-cavity configuration [42]. The oscillator was single frequency and tunable from 874 to 936 nm, with maximum output of 20 mW at 930 nm. The pump power after the amplifier and two pairs of optical isolators was more than 2 W. With 1.5 W of laser-diode power, 60 mW of second harmonic generation at 465 nm was produced, given a normalized conversion efficiency

of 2.8%/W. An improved efficiency of 3.4%/W was obtained by expansion and spatial filtering of the diode beam before it was focused into the periodically poled CLN [42].

10.3 2.6 μm patterning in lithium tantalate

We have applied the optimized method for 2.6-μm periodical poling of the CLT 0.3-mm-thick substrates. It is seen that the domain patterns on $\mathbf{Z}^+$ are practically ideal (Fig. 83). Such domain structure was prepared in fragments of 2-inch-diameter substrate. The detail optical testing of the obtained domain structures will be done later.

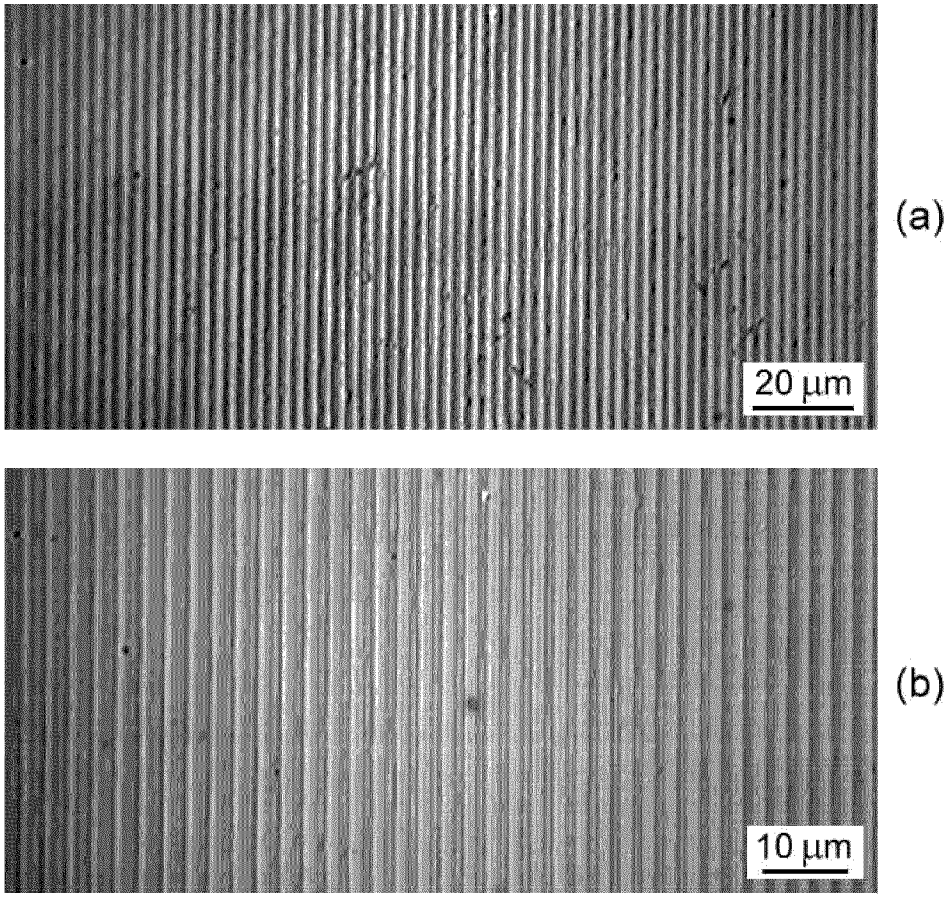

Figure 83 Domain patterns in CLT for 2.6-μm-period for $\mathbf{Z}^+$ view revealed by etching and visualized by optical microscopy.

11 Recommendation

The new important information about the domain kinetics in congruent and stoichiometric LN and LT during backswitched poling was obtained as a result of aforementioned investigations. The real-time observation of the domain kinetics during poling in both crystals is a new powerful instrument for optimization of the poling technique. The modified poling process allows to produce for the first time the bulk domain patterns with 2.6-μm-period in 0.5-mm-thick CLN and

0.3-mm-thick CLT substrates. It was shown that backswitched poling enables higher fidelity and shorter period domain patterning. The poling of thick substrates can be achieved easily in SLT crystals. The proposed technology based on the controlled backswitching process demonstrates the new possibilities in the domain engineering. The first achievements in domain frequency multiplication and nanodomain engineering show the way to overcome the micron-period barrier in domain patterning.

The future progress in periodical patterning requires the development of such activity for patterning of thicker substrates of stoichiometric and doped LN and LT produced by different techniques.

12 References

[1] R.L. Byer, *J. of Nonlinear Optical Physics & Materials*, **6**, 549 (1997).

[2] K. Mizuushi and K. Yamamoto, *Opt.Lett.*, **21**, 107 (1996).

[3] J.-P. Meyn and M.M. Fejer, *Opt.Lett.*, **22**, 1214 (1997).

[4] M. Yamada, N. Nada, M. Saitoh, and K. Watanabe, *Appl.Phys.Lett.*, **62**, 435 (1993).

[5] J.U. Kang, W.K. Burns, Y.J. Ding, and J.S. Melinger, *presented at the Conference on Lasers and Electro-Optics, Baltimore, Maryland, May 18-23*, (1997).

[6] W.P. Risk and S.D. Lau, *Appl.Phys.Lett.*, **69**, 3999 (1996).

[7] G.D. Miller, R.G. Batchko, W.M. Tulloch, D.R Weise, M.M. Feier, and R.L. Byer, *Opt.Lett.*, **22**, 1834 (1997).

[8] E. Fatuzzo and W.J. Merz, *Phys. Rev.*, **116**, 61 (1959).

[9] G.W. Taylor, *J. Appl. Phys.*, **37**, 593 (1966).

[10] V.Ya. Shur, A.L. Gruverman, V.P. Kuminov, and N.A. Tonkachyova, *Ferroelectrics*, **111**, 197 (1990).

[11] V.Ya. Shur, Yu.A. Popov, and N.V. Korovina, *Sov. Phys. Solid State*, **26**, 471 (1984).

[12] V.Ya. Shur, in *Ferroelectric Thin Films: Synthesis and Basic Properties*, New York: Gordon&Breach, ch. 6, pp. 153-192 (1996).

[13] V.Ya. Shur and E.L. Rumyantsev, *Ferroelectrics*, **191**, 319 (1997).

[14] A.L. Alexandrovski, G. Foulon, L.E. Myers, R.K. Route, and M.M. Fejer, SPIE Proceedings on Laser Material Crystal Growth and Nonlinear Materials and Devices, 3610, 44 (1999)

[15] K. Kitamura, Y. Furukawa, K. Niwa, V. Gopalan, and T.E. Mitchell, *Appl. Phys.Lett.*, **73**, 3073 (1998).

[16] K. Kitamura, Y. Furukawa, and N. Iyi, *Ferroelectrics*, **202**, 21 (1997).

[17] L.E. Myers, R.C. Eckardt, M.M. Fejer, R.L. Byer, and W.R. Bosenberg, *Optic Letters*, **21**, 591 (1996).

[18] G.D. Miller, R. G. Batchko, M. M. Fejer, and R. L. Byer, *SPIE Proceedings on Solid State Lasers and Nonlinear Crystals*, **2700**, 34 (1996).

[19] A. Gruverman, O. Auciello, and H. Tokumoto, *Appl. Phys. Lett.,* **69**, 3191 (1996).

[20] A. Gruverman, O. Auciello, R. Ramesh, and H. Tokumoto, *Nanotechnology,* **8**, A38 (1997).

[21] P.V. Lambeck and G.H. Jonker, *Ferroelectrics*, **22**, 729 (1978).

[22] V.M. Fridkin, *Ferroelectrics Semiconductors*, (New York and London: Consultants Bureau, 1980), 264 p.

[23] W.J. Merz, *Phys. Rev.*, **95**, 690 (1954).

[24] V.Ya. Shur, E.V. Nikolaeva, E.L. Rumyantsev, E.I. Shishkin, A.L. Subbotin, and V.L. Kozhevnikov, *Ferroelectrics*, **222**, 323 (1999).

[25] V.Ya. Shur, E.L. Rumyantsev, V.P. Kuminov, A.L. Subbotin, and V.L. Kozhevnikov, *Phys. Solid State*, **41**, 269 (1999).

[26] V. Gopalan and T. Mitchell, *J. Appl. Phys.,* **83**, 941 (1998).

[27] A.N. Kolmogorov, *Izv. Acad. Nauk USSR., Ser Math.*, **3**, 355 (1937).

[28] M. Avrami, *J. Chem. Phys.,* **7**, 1103 (1939); **8**, 212 (1940); **9**, 177 (1941).

[29] V.Ya. Shur, E.L. Rumyantsev, and S.D. Makarov, *J. Appl. Phys.,* **84**, 445 (1998).

[30] M.E. Lines and A.M. Glass, *Principles and application of ferroelectrics and related materials*, Clarendon Press, Oxford, 1977, 736p.

[31] V.Ya. Shur, E.L. Rumyantsev and A.L. Subbotin, *Ferroelectrics*, **140**, 305 (1993).

[32] V.Ya. Shur and E.L. Rumyantsev, *J.Kor.Phys.Soc.*, **32**, S727 (1998).

[33] L.E. Myers, *Quasi-Phasematched Optical Parametric Oscillators In Bulk Periodically Poled Lithium Niobate*, Ph. D. thesis, The Stanford University, 1995.

[34] V.Ya. Shur, A.L. Gruverman, V.V. Letuchev, E.L. Rumyantsev, and A.L. Subbotin, *Ferroelectrics*, **98**, 29 (1989).

[35] V.Ya. Shur, A.L. Gruverman, and E.L. Rumyantsev, *Ferroelectrics*, **111**, 123 (1990).

[36] V.Ya. Shur and E.L. Rumyantsev, *Ferroelectrics*, **142**, 1 (1993).

[37] V.Ya. Shur, R.G. Batchko, E.L. Rumyantsev, G.D. Miller, M.M. Fejer, and R.L. Byer, *Proc. 11th ISAF, Piscataway, NJ: IEEE*, 399 (1999).

[38] R.G. Batchko, G.D. Miller, V.Ya. Shur, E.L. Rumyantsev, M.M. Fejer, and R.L. Byer, *SPIE Proceedings on Laser Material Crystal Growth and Nonlinear Materials and Devices*, **3610**, 36 (1999).

[39] R.G. Batchko, V.Ya. Shur, M.M. Fejer, and R.L. Byer, *Appl.Phys.Letters*, **75**, 1673 (1999).

[40] R.G. Batchko, M.M. Fejer, R.L. Byer, V.Ya. Shur, and L. Erman, *OSA Trends in Optics and Photonics Series*, **26**, Advanced Solid-State Lasers, M.M. Fejer, H. Injeyan and U. Keller (eds.), 707 (1999).

[41] R.G. Batchko, M.M. Fejer, R.L. Byer, V.Ya. Shur, and W.S. Capinski, *1999 OSA Technical Digest Series* (Optical Society of America, Washington, D.C., 1999), 353.

[42] R.G. Batchko, M.M. Fejer, R.L. Byer, D. Woll, R. Wallenstein, V.Ya. Shur, and L. Erman, *Opt.Lett.*, **24**, 1293 (1999).

Presentations

1. V.Ya. Shur, R.G. Batchko, E.L. Rumyantsev, G.D. Miller, M.M. Fejer, and R.L. Byer, Domain Engineering: Periodic Domain Patterning in Lithium Niobate, *Proc. 11th ISAF, Piscataway, NJ: IEEE*, 399-406 (1999).
2. V.Ya. Shur, E.L. Rumyantsev, R.G. Batchko, G.D. Miller, M.M. Fejer, and R.L. Byer, Domain Kinetics during Periodic Domain Patterning in Lithium Niobate, *Phys. Solid State*, **41**, N.10, 1681-1687 (1999).
3. V. Shur, E. Rumyantsev, R. Batchko, G. Miller, M. Fejer, and R. Byer, Physical Basis of the Domain Engineering in the Bulk Ferroelectrics, *Ferroelectrics*, **221**, 157-167 (1999).
4. R.G. Batchko, G.D. Miller, V.Ya. Shur, E.L. Rumyantsev, M.M. Fejer, and R.L. Byer, Domain Patterning in Lithium Niobate Using Spontaneous Backswitching, *SPIE Proceedings on Laser Material Crystal Growth and Nonlinear Materials and Devices*, **3610**, 36-43 (1999).
5. R.G. Batchko, V.Ya. Shur, M.M. Fejer, and R.L. Byer, Backswitch Poling in Lithium Niobate for High-fidelity Domain Patterning and Efficient Blue Light Generation, *Appl.Phys.Letters*, **75**, 1673-1675 (1999).
6. R.G. Batchko, M.M. Fejer, R.L. Byer, V.Ya. Shur, and L. Erman, Backswitch Poling of 0.5-mm-thick Lithium Niobate for 6.4%/W-efficient CW Second Harmonic Generation of 460 nm Light, *OSA Trends in Optics and Photonics Series*, **26**, Advanced Solid-State Lasers, M.M. Fejer, H. Injeyan and U. Keller (eds.), 707-708 (1999).
7. R.G. Batchko, M.M. Fejer, R.L. Byer, V.Ya. Shur, and W.S. Capinski, 59%-efficient CW-modelocked Second Harmonic Generation of Blue Light in Backswitch-poled Lithium Niobate, *1999 OSA Technical Digest Series* (Optical Society of America, Washington, D.C., 1999), 353.
8. R.G. Batchko, M.M. Fejer, R.L. Byer, D. Woll, R. Wallenstein, V.Ya. Shur, and L. Erman, Continuous-Wave Quasi-phasematched Generation of 60 mW at 465 nm by Single-pass Frequency-doubling of a Laser Diode in Backswitch-poled Lithium Niobate, *Optic Letters*, **24**, 1293-1295 (1999).
9. V.Ya. Shur, E.L. Rumyantsev, E.V. Nikolaeva, E.I. Shishkin, D.V. Fursov, R.G. Batchko, L.A. Eyres, M.M. Fejer, and R.L. Byer, Nanoscale Domain Patterning during Spontaneous Backswitching in Lithium Niobate, *Appl. Phys. Lett.* (in press).
10. V.Ya. Shur, E.L. Rumyantsev, E.V. Nikolaeva, E.I. Shishkin, R.G. Batchko, G.D. Miller, M.M. Fejer, and R.L. Byer, Regular Ferroelectric Domain Array in Lithium Niobate Crystals for Nonlinear Optic Applications, *Ferroelectrics* (in press)
11. V.Ya. Shur, E.L. Rumyantsev, E.V. Nikolaeva, E.I. Shishkin, R.G. Batchko, L.A. Eyres, M.M. Fejer, and R.L. Byer, Self-Organizing Formation of Non-Equilibrium Nanodomain Patterns during Backswitching in Lithium Niobate, *Phys. Rev. Lett.* (submitted).
12. V.Ya. Shur, E.L. Rumyantsev, E.V. Nikolaeva, E.I. Shishkin, R.G. Batchko, L.A. Eyres, M.M. Fejer, and R.L. Byer, Formation of the Organized Structures of Nanodomains during Spontaneous Backswitching in Lithium Niobate, *Abstracts of Second Russian Seminar on Nonlinear Processes and Self-organization in Material Science*, Voronez, February 3-5, 1999 (**invited lecture**).

13. R.G. Batchko, M.M. Fejer, R.L. Byer, V.Ya. Shur, and L. Erman, Backswitch Poling of 0.5-mm-thick Lithium Niobate for 6.4%/W-efficient CW Second Harmonic Generation of 460 nm Light, *ASSL'99-TOPS'99,* January – February 1999.
14. R.G. Batchko, M.M. Fejer, R.L. Byer, V.Ya. Shur, and W.S. Capinski, 59%-efficient CW-modelocked Second Harmonic Generation of Blue Light in Backswitch-poled Lithium Niobate, *CLEO'99*, Baltimore, May 1999.
15. V.Ya. Shur, E.L. Rumyantsev, R.G. Batchko, G.D. Miller, M.M. Fejer, and R.L. Byer, Regular Ferroelectric Domain Array in Lithium Niobate Crystals for Nonlinear Optic Applications, *9th European Meeting on Ferroelectricity*, Praha, Czech Republic, 12-16 July, 1999 (**invited lecture**)
16. V.Ya. Shur, E.L. Rumyantsev, E.V. Nikolaeva, E.I. Shishkin, D.V. Fursov, R.G. Batchko, L.A. Eyres, M.M. Fejer, and R.L. Byer, Self-Organizing Formation of Nanodomain Patterns during Spontaneous Backswitching in Lithium Niobate, *9th European Meeting on Ferroelectricity, Praha, Czech Republic*, 12-16 July, 1999.
17. V.Ya. Shur, E.L. Rumyantsev, R.G. Batchko, G.D. Miller, M.M. Fejer, and R.L. Byer, Physical Basis of Periodic Domain Patterning in Lithium Niobate, *15th Russian National Conference on Physics of Ferroelectrics*, Rostov-on-Don, September 14-18, 1999 (**invited lecture**).
18. V.Ya. Shur, E.L. Rumyantsev, E.V. Nikolaeva, E.I. Shishkin, D.V. Fursov, R.G. Batchko, G.D. Miller, M.M. Fejer, and R.L. Byer, Kinetics of the Domain Structure during Polarization Reversal in Lithium Niobate*, 15th Russian Conference on Physics of Ferroelectrics*, Rostov-on-Don, September 14-18, 1999.
19. V.Ya. Shur, E.L. Rumyantsev, E.I. Shishkin, E.V. Nikolaeva, M.V. Kalinina, D.V. Fursov, R.G. Batchko, G.D. Miller, M.M. Fejer, and R.L. Byer, Self-organized Formation of Nano-domain Structures in Lithium Niobate, *15th Russian Conference on Physics of Ferroelectrics*, Rostov-on-Don, September 14-18, 1999.
20. V.Ya. Shur, E.L. Rumyantsev, E.V. Nikolaeva, E.I. Shishkin, R.G. Batchko, G.D. Miller, M.M. Fejer, and R.L. Byer, Domain Engineering in Lithium Niobate and Lithium Tantalate, *CNOM meeting,* September 24 - 25, 1999 (**invited lecture**).
21. R.G. Batchko, A.L. Alexandrovski, M.M. Fejer, R.L. Byer, V.Y. Shur, and W.S. Capinski, Generation of Blue Light by Frequency-doubling a Modelocked Ti:sapphire Laser in Periodically-polled Lithium Niobate, *CNOM meeting*, September 24 - 25, 1999.
22. R.G. Batchko, V.Y. Shur, M.M. Fejer, and R.L. Byer, Backswitch-Poling: a Simple and Practical Solution to High-fidelity Ferroelectric Domain Engineering, *1999 OSA Annual Meeting*: Optics in High-Tech Industries, Santa Clara, CA, September 26-30, 1999, p.130.